Article

Effects of topography on dynamics and mass loss of lake-terminating glaciers in southern Patagonia

Masahiro Minowa[1] (ID), Marius Schaefer[2] (ID) and Pedro Skvarca[3]

[1]Institute of Low Temperature Science, Hokkaido University, Kita-19, Nishi-8, Sapporo 060-0819, Japan; [2]Instituto de Ciencias Físicas y Matemáticas, Universidad Austral de Chile, Valdivia, Chile and [3]Glaciarium—Glacier Interpretive Center, El Calafate, Santa Cruz, Argentina

Abstract

Calving glaciers are highly sensitive to bedrock geometry near their terminus. To understand the mechanisms controlling rapid calving glaciers' mass loss, we measured the lake topography in front of four lake-terminating glaciers in the southern Patagonian icefield. Using remotely sensed surface elevation data, we calculated flotation height and surface slope and compared those with changes in ice-front position, surface speed and surface elevation. Rapid retreat accompanied by rapid flow acceleration and ice surface steepening was observed at Glaciar Upsala from 2008–2011, and at O'Higgins and Viedma glaciers from 2016–present. Surface lowering in the lower part of Glaciar Upsala reached $30 \, \mathrm{m \, a^{-1}}$ and was $18 \, \mathrm{m \, a^{-1}}$ and $12 \, \mathrm{m \, a^{-1}}$ at O'Higgins and Viedma glaciers, respectively. Near- or super-buoyant conditions were observed prior to these events, leading to gradual flow acceleration due to low effective pressure and decoupling from the bed. The super-buoyant condition and gradual acceleration imply full-thickness buoyant calving, which causes the ice front to retreat from the shallow bedrock topography with substantial flow acceleration. We conclude that the buoyancy force plays an important role in the rapid mass loss of lake-terminating glaciers in southern Patagonia.

1. Introduction

The majority of temperate ice masses in the southern hemisphere can be found in Patagonia, between 46.5°S and 51.5°S, home to dynamic calving glaciers (Aniya and others, 1997). The northern and southern Patagonian icefields are the two main ice masses in the region, covering ∼3,700 km² and ∼12,000 km², respectively (Meier and others, 2018). They are losing ice mass at one of the highest rates in the world (Hugonnet and others, 2021). This is because lake- and ocean-terminating glaciers dominate 80% of the outlet glaciers (Aniya and others, 1997). These calving glaciers lose ice mass not only at the ice surface but also at their terminus through frontal ablation, consisting of iceberg calving and subaqueous melting (e.g. Truffer and Motyka, 2016). The number of lake-terminating glaciers in both icefields accounts for more than 70% of calving glaciers and constitutes 74% of the mass loss from the icefields (e.g. Minowa and others, 2021). These lake-terminating glaciers in Patagonia flow at a high rate ranging from several hundred metres to kilometres per year (Sakakibara and Sugiyama, 2014; Mouginot and Rignot, 2015), and have shown heterogeneous fluctuation over the last few decades (e.g. Aniya and others, 1997; Sakakibara and Sugiyama, 2014). Therefore, understanding the mechanisms of ice mass change in lake-terminating glaciers is important for interpreting the current and future mass changes of Patagonian glaciers.

Ice dynamics play a major role in the mass change of calving glaciers (e.g. Meier and Post, 1987; O'Neel and others, 2005; Bevan and others, 2012; Felikson and others, 2017). This is because the ice flow at the lower reach of a calving glacier is primarily determined by basal sliding, which relates to driving stress and inversely relates to effective pressure (Sugiyama and others, 2011; Doyle and others, 2018; Christmann and others, 2021). The driving stress is controlled by ice thickness and surface slope. The effective pressure is defined as the difference between overburden ice pressure and hydraulic subglacial water pressure. The greatest ice flow is found near the terminus of a calving glacier, where effective pressure is usually small. Thus, the acceleration of ice flow at the terminus extends and thins the glacier, i.e. causes dynamic thinning, which steepens the ice surface and further accelerates the ice flow by increasing driving stress and reducing effective pressure (Benn and others, 2007). Ice flow acceleration causes more ice fracture and calving, resulting in ice front retreat. For example, Columbia Glacier in Prince William Sound has retreated by ∼20 km since the 1980s accompanied by flow acceleration and thinning (O'Neel and others, 2005). The retreat was controlled by overdeepening basins (Meier and Post, 1987), often formed by glacial erosion (Cook and Swift, 2012). This is because effective pressure decreases substantially when glaciers get close to floating by decreasing basal drag and causing ice flow acceleration (Kamb and others, 1994; Meier and others, 1994; O'Neel and others, 2005). Once the ice front retreats into a deeper basin, instability takes place by losing buttressing effect, increasing ice flow and enhancing calving rate (Benn and others, 2007). Moreover, modelling (Nick and others, 2009; Enderlin and Howat, 2013; Frank and others, 2022) and theoretical studies (e.g. Weertman, 1974;

Pfeffer, 2007) have also strongly suggested the topography influence on the dynamic calving glacier's retreat. Therefore, knowing the ice flow acceleration and iceberg calving mechanisms, and their relation to topography are essential to understand the rapid mass loss of calving glaciers (e.g. Benn and others, 2007; Truffer and Motyka, 2016; Benn and others, 2017; Felikson and others, 2017; Catania and others, 2018).

Buoyancy force plays an important role in the increase in ice speed and iceberg calving (Meier and Post, 1987; O'Neel and others, 2005; Benn and others, 2007; Stearns and Van der Veen, 2018). Because the calving front of an ocean-terminating glacier is often highly fractured and not strong enough to accommodate buoyancy force, it causes very large calving events, as has been observed in the ocean-terminating glaciers in Alaska (Walter and others, 2010) and in Greenland (Amundson and others, 2008; James and others, 2014; Murray and others, 2015). It appears that the recent thinning of calving glaciers results in the front being more vulnerable to buoyancy force, which triggers large-scale calving in Greenland (van Dongen, 2021). Furthermore, large-scale calving can initiate flow acceleration by changing the force-balance near the terminus (Amundson and others, 2022; Ultee and others, 2022). It has also been reported that the importance of buoyancy force for glacier calving on retreat in the lake-terminating glaciers. Several studies in Patagonia (Naruse and Skvarca, 2000; Warren and others, 2001) and Alaska (Boyce and others, 2007) suggested that transiently floating tongues can form because the lake-terminating glaciers have fewer fractures (e.g. less flow speed, tidal flexure and low subaqueous melting). For just such a transient floating tongue at Glaciar Nef, Patagonia, Warren and others (2001) argued that buoyancy force acts on the tongue to cause tensile stress at the base of a glacier, resulting in a basal crevasse and catastrophic iceberg calving events. Boyce and others (2007) reported that the floating ice front of Mendenhall Glacier, Alaska, lasted about two years before it calved due to a small increase in lake level (i.e. an increase in buoyancy force). More recently, a large-scale buoyancy-driven calving was documented at Glaciar Grey, a lake-terminating glacier in Patagonia (Sugiyama and others, 2019). Therefore, knowing the floating condition near the ice front provides crucial information on how the buoyancy force influences the dynamic glacier retreat.

In lake-terminating glaciers in Patagonia, ice flow acceleration has been postulated to be the cause of the rapid retreat and thinning observed (e.g. Naruse and others, 1997; Rignot and others, 2003; Sakakibara and others, 2013; Sakakibara and Sugiyama, 2014; Mouginot and Rignot, 2015; Abdel Jaber and others, 2019). These studies have also suggested that the bed topography near the terminus is essential for the observed rapid retreat. However, bedrock topography data near the terminus of calving glaciers is limited in Patagonia (Gourlet and others, 2016; Millan and others, 2019). A field survey of lake geometry and a detailed comparison between glacier dynamics and geometry can provide insight into the mechanisms which accelerate ice flow. It can also increase our understanding about the importance of the rapid dynamic retreat for the glacier mass budget by increasing iceberg calving.

In this study, we present the lake topography measured near the terminus of four lake-terminating glaciers: O'Higgins, Viedma, Upsala and Tyndall glaciers. These glaciers are located on the eastern side of the southern Patagonian icefield ranging from 48.5°S and 51.5°S (Fig. 1). We analysed ice-front position, surface speed and surface elevation change between 2000 and 2021, using variable optical remote sensed imagery, which we compared with geometry near the termini. Particularly, we calculated the height above buoyancy near the ice front using bed topography and ice surface elevation to discuss how ice flow and calving change under near buoyant and buoyant conditions. Our study helps to understand the mechanisms of the rapid retreat and mass loss of lake-terminating glaciers in Patagonia.

2. Study site

2.1 Glaciar O'Higgins

Glaciar O'Higgins is the fourth largest glacier in the southern Patagonian icefield, covering $762\,km^2$ (De Angelis, 2014). The surface elevation of the glacier ranges from 3,200 m at Volcán Lautaro to 252 m at O'Higgins/Lago San Martin (Fig. 1). The glacier width near the terminus is ~2.5 km (Fig. 1). Historical aerial photograph analysis shows that the glacier has experienced a rapid ice front retreat of approximately 15 km over almost a century since 1896 (Casassa and others, 1997) when the ice front passed deep water ~800 m (Schaefer and others, 2011). After the rapid retreat, the retreat rate decreased to $36\,m\,a^{-1}$ between 1984 and 2000 and to $17\,m\,a^{-1}$ between 2000 and 2011 (Sakakibara and Sugiyama, 2014). The ice flow speed in the lower ablation area shows it to have the fastest speed among the lake-terminating glaciers in Patagonia, probably due to the steep surface slope (Sakakibara and Sugiyama, 2014; Mouginot and Rignot, 2015). Its speed was close to $5\,km\,a^{-1}$ near the terminus in 1984, which decreased substantially down to $2\,km\,a^{-1}$ in 2014 (Mouginot and Rignot, 2015). The ice volume change rate is $-0.89\,km^3\,a^{-1}$ between 2000 and 2012 and $-0.85\,km^3\,a^{-1}$ between 2012 and 2016 (Abdel Jaber and others, 2019).

2.2 Glaciar Viedma

Glaciar Viedma is the second-largest glacier in the southern Patagonian icefield (De Angelis, 2014), covering $974\,km^2$ in area and shares its accumulation area with Pío XI, O'Higgins, Chico and Upsala glaciers (Fig. 1). The glacier flows into Lago Viedma (252 m a.s.l.) at a flow speed of ~1 km a^{-1} near the ~1.5 km wide terminus (Sakakibara and Sugiyama, 2014). The retreat rate of the ice-front position was $30\,m\,a^{-1}$ between 1984 and 2000 and $41\,m\,a^{-1}$ between 2000 and 2011 (Sakakibara and Sugiyama, 2014). Lake water depth was measured in the summer of 2012 and 2013 near the terminus of the glacier (Sugiyama and others, 2016). These measurements showed an increased water depth towards the ice front with a maximum depth of ~390 m close to the front. The ice volume change rate is $-1.95\,km^3\,a^{-1}$ between 2000 and 2012, which slightly increased to $-2.3\,km^3\,a^{-1}$ between 2012 and 2016 (Abdel Jaber and others, 2019).

2.3 Glaciar Upsala

Glaciar Upsala is one of the most well-studied glaciers in the region. Fieldwork and remote sensing data revealed a rapid retreat (e.g. Warren and others, 1995b; Naruse and others, 1997; Skvarca and Naruse, 1997; Skvarca and others, 2002, 2003; Muto and Furuya, 2013; Sakakibara and others, 2013; Mouginot and Rignot, 2015; Sakakibara, 2016; Abdel Jaber and others, 2019). The glacier covers $835\,km^2$ of the southern Patagonian icefield (De Angelis, 2014) and flows into Brazo Upsala (177.5 m a.s.l.), a northwestern arm of Lago Argentino, at a rate of 2 km a^{-1} near the ~3 km wide terminus (Sakakibara and Sugiyama, 2014). Early studies reported that rapid retreat occurred in the 90 s when the ice front retreated up to $700\,m\,a^{-1}$ and ice thinning reached $11\,m\,a^{-1}$ in the eastern half of the glacier (Skvarca and others, 1995). It was suggested that the dynamic thinning caused the rapid retreat (Naruse and others, 1997; Skvarca and others, 2002). Another rapid retreat occurred in 2008, and the changes in ice-front position, surface elevation, and ice speed were
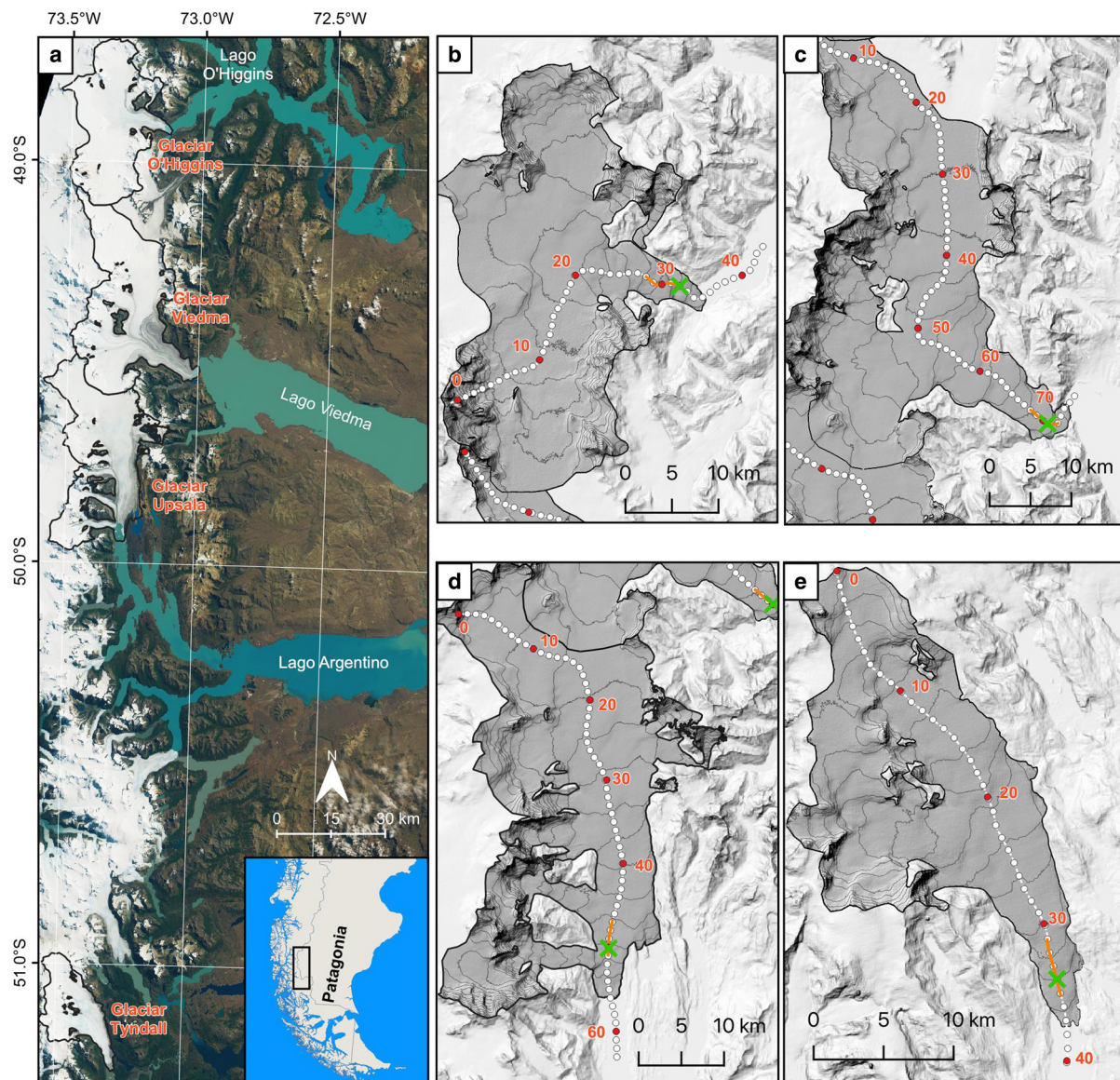
Figure 1. (a) Satellite images showing the study area. Glacier basins in 2000 are indicated by black lines. Satellite images are taken by Sentinel-2A on March 3 2021, composed by sentinelflow (Seguinot, 2020). Topographic maps of (b) O'Higgins, (c) Viedma, (d) Upsala and (e) Tyndall glaciers with 100 m contour intervals. The centreline of each glacier is indicated by white and red circles, dotted every 1 and 10 km, respectively, and starts from the head of the glacier towards down-glacier. Orange lines and green crosses indicate the place where the mean surface elevation and ice speed were obtained, respectively.

documented by Sakakibara and others (2013), who also reported that the glacier has retreated 2.9 km, accelerated 20–50% between 2008 and 2011 and the thinning rate reached 39 m a^{-1} between 2006 and 2010. Lake water topography over the region where the rapid retreat occurred was reported by Sugiyama and others (2016) but has not yet been compared with the glacier fluctuation. The maximum depth along the Brazo Upsala arm ranged between 560 and 580 m. Due to this rapid retreat and acceleration, the volume change rate is the largest in Patagonia between 2000 and 2012 at −2.8 km^3 a^{-1}, which slightly decreased to −2.5 km^3 a^{-1} between 2012 and 2016 (Abdel Jaber and others, 2019).

2.4 Glaciar Tyndall

Glaciar Tyndall is located in the southernmost part of the southern Patagonian icefield (Fig. 1), covering 309 km^2 of the icefield (De Angelis, 2014). The glacier flows into Lago Geike (40 m a.s.l.), which is a small proglacial lake, compared with other lakes described above (Fig. 1a). The flow speed is about 500 m a^{-1} near the ~2 km wide terminus, which is also lower than at the

other three glaciers. The glacier has shown continuous retreat and thinning over several decades (Naruse and others, 1987; Kadota and others, 1992; Nishida and others, 1995; Rivera and Casassa, 2004; Raymond and others, 2005; Sakakibara and Sugiyama, 2014). For example, the retreat rate was 80 m a^{-1} between 1986 and 2000, and 135 m a^{-1} between 2000 and 2011, while no significant ice speed variation was reported during those periods (Sakakibara and Sugiyama, 2014). A bathymetry survey of Lago Geike was performed in 2001 (Raymond and others, 2005). A traverse profile in the lake a few hundred metres from the ice front showed a U-shaped profile with a maximum depth of about 350 m (Fig. 4 in Raymond and others (2005)). The ice volume change rate is −0.79 km^3 a^{-1} between 2000 and 2012, which slightly decreased to −0.48 km^3 a^{-1} between 2012 and 2016 (Abdel Jaber and others, 2019).

3. Materials and methods

An overview of the available dataset used in this study is summarized in Figure 12.

3.1 Lake bathymetry

The water depth measurements were repeated in sections of glacier retreat at Lago Viedma and Brazo Upsala after previous measurements were taken in 1998 and 1999 (Skvarca and others, 2002) and again in 2012, 2013 and 2014 (Sugiyama and others, 2016) (Fig. 2). Water depth was measured in January 2017, November 2018, November 2019 and June 2020 in Lago Viedma, and November 2019 and March 2020 in Brazo Upsala (Fig. 12). We also performed a water depth observation at Lago O'Higgins in February 2020 and Lago Geike in October 2019 (Figs 2 and 12). While water depth sounding was carried out with a kayak at Lago Geike due to a lack of regular boat operations, a small boat was used to conduct measurements in the other lakes. We used a depth sounder (Lowrance HDS-7) operated with an 80 kHz frequency-modulated transducer (Airmar B75M). The horizontal coordinates were obtained by a built-in single-frequency GPS. Water depth, horizontal coordinates and echograms were recorded every 1 sec. The uncertainty of the observed depth was estimated in the previous studies to be 5.7 m, or 3.7% of the observed depth by comparing the depth obtained using a water pressure sensor (Sugiyama and others, 2016, 2021), while the error in horizontal coordinates is expected to be several metres. To generate a bathymetry map, we compiled our observations with the early observations of the lake topography at Lago Viedma and Brazo Upsala (Skvarca and others, 2002; Sugiyama and others, 2016). Finally, irregular depth datasets were interpolated into a 50 m grid matrix with a conventional natural neighbouring interpolation method (Watson, 1999).

3.2 Ice front position, surface speed and surface elevation

We extended observations of the ice-front position, surface speed and surface elevation obtained in the previous studies (Sakakibara and Sugiyama, 2014; Minowa and others, 2021). We analysed Landsat 8 images between 2019 and 2021 and Sentinel-2 images between 2016 and 2021. The ice-front position was manually delineated on a geographic information system using true-colour images (Fig. 12). The composite images generated by Landsat 8
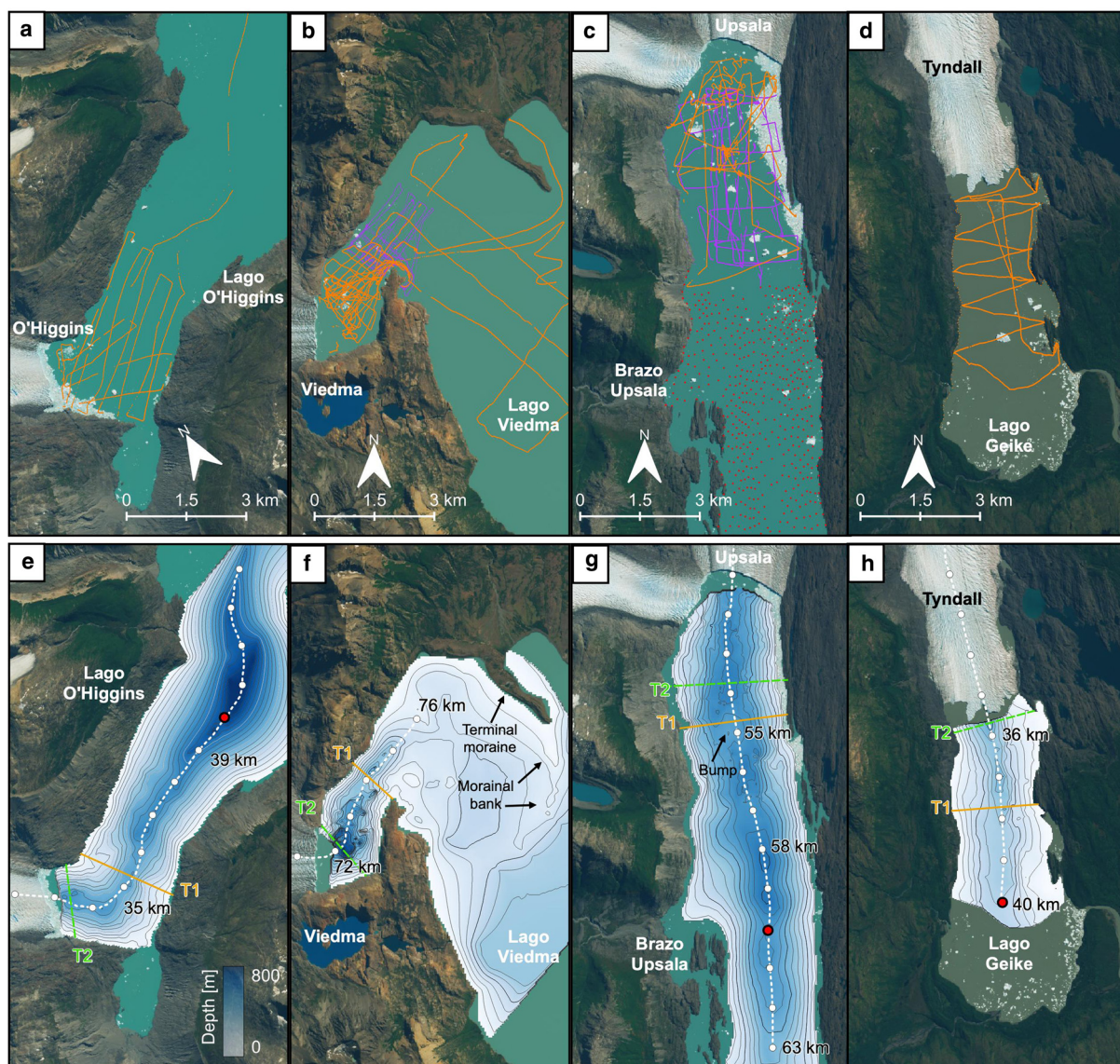

Image: Sentinel-2A, March 3, 2021

Figure 2. Orange lines indicate the survey lines of water depth in this study in front of (a) O'Higgins, (b) Viedma, (c) Upsala and (d) Tyndall glaciers. Purple lines and red dots indicate previous bathymetry observations by Sugiyama and others (2016) and Skvarca and others (2002). Generated bathymetry map is indicated for (e) O'Higgins, (f) Viedma, (g) Upsala and (h) Tyndall glaciers. Water depth contour intervals are every 50 m. Two cross-sectional profiles were obtained along solid orange and dashed green lines denoted T1 and T2, chosen to cross the shallowest and the deepest parts of the lake, which have appeared after the recent glacier's retreat since 2000. The background satellite image was acquired by Sentinel-2A on March 3, 2021.

and Sentinel-2 have 30 and 10 m resolutions, respectively. Combining the ice-front position mapped in the previous studies (Sakakibara and Sugiyama, 2014; Minowa and others, 2021), our study covers variations in the ice-front position since the 1970s.

The optical images were also used to calculate the surface ice speed. For Landsat 8, we applied the feature-tracking method developed for analysing Landsat images in the previous study (Sakakibara and Sugiyama, 2014). The programming code uses the orientation correlation method in the frequency domain to measure displacement (Haug and others, 2010; Heid and Kääb, 2012). For Sentinel-2 images, we applied the same method but with a different toolbox called ImGRAFT (Messerli and Grinsted, 2015). Temporal separation of the images was set to be between 16 and 60 days for Landsat 8 and between 10 to 60 days for Sentinel-2. Uncertainty in the ice speed measurement was analysed regarding co-registration errors, ambiguity in the cross-correlation peak and false correlation. The first two errors were accounted for by taking misfits between two images on bedrock areas, and the last error was evaluated for each grid (Sakakibara and Sugiyama, 2014). The sum of these errors ranges from 0.02 and 0.7 km a^{-1} with 0.19 km a^{-1} on average. Further technical details can be found in previous studies (Sakakibara and Sugiyama, 2014; Messerli and Grinsted, 2015). In addition to the ice speeds obtained in this study, we used previously reported ice speeds over the southern Patagonian icefield between 2000 and 2019 (Sakakibara and Sugiyama, 2014; Minowa and others, 2021).

Surface elevation change and slope were measured with digital elevation models (DEM) obtained by Shuttle Radar Topography Mission (SRTM), the Advanced Spaceborne Thermal Emission and Reflection Radiometer (ASTER) and the Japanese Advanced Land Observation Satellite (ALOS). We used SRTM v3 DEM, which was acquired in February 2000. ASTER-VA DEM products were acquired between 2001 and 2022 for 17, 30, 25 and 9 DEMs for O'Higgins, Viedma, Upsala and Tyndall glaciers, respectively. We generated 6 DEMs from ALOS stereo images with a rational polynomial coefficient by Ames Stereo Pipeline (ASP) version 3.0 (Shean and others, 2016). ASP is an automated and open-source photogrammetry software consisting of image alignment, correlation and raster conversion workflows. We used the More Global Matching algorithm implemented in ASP for image correlation. The nadir- and forward-looking or nadir- and backward-looking image pair with a processing level of 1B2 (geometrically corrected data) were processed. Two ALOS DEMs were available for Glaciar Upsala, and the rest of the glaciers have one DEM each. The spatial resolution of DEMs was 30 m for SRTM, ASTER-VA and ALOS. All DEMs were georeferenced to SRTM DEM with an iterative method (Nuth and Kääb, 2011). Uncertainties in DEMs were estimated over the ice-free regions where elevation differences were assumed to be negligible. The standard deviation between SRTM and ASTER-VA DEMs, and between SRTM and ALOS DEMs was 11 m on average.

To visualize ice speed, spatial surface elevation and slope, we interpolated them into the centrelines along each glacier. The centreline was manually determined to follow the middle of the glacier along the glacier where surface ice speed shows maximum. The locations along the centreline are defined as km 0 at the head of the glacier (Fig. 1). The temporal variations in surface ice speed, surface elevation and surface slope were sampled near the terminus for individual glaciers. The median ice speed was calculated from 3 × 3 grids, interpolated at a fixed location at 32, 71, 40 and 34 km of the centreline for O'Higgins, Viedma, Upsala and Tyndall glaciers, individually (Green cross in Fig. 1). For the ice speed, locations were chosen where the speed was obtained continuously. Near the ice front this is
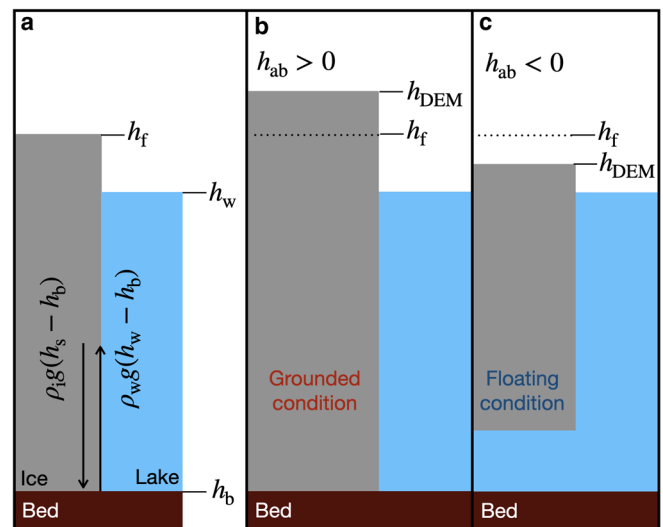

Figure 3. (a) Illustration of the overburden ice pressure and buoyancy force. (b) A higher ice surface elevation (h_{DEM}) than the flotation height (h_f) suggests a grounded condition, (c) while a lower h_{DEM} than h_f implies a floating condition. h_{ab}—height above buoyancy, h_w—water level, h_b—bed elevation, ρ_w—water density, ρ_i—ice density and g—gravitational acceleration.

often not possible due to limited correlation caused by high ice speed and fractures. The mean surface elevation and surface slope were calculated along the centreline over a distance of 4 km towards upglacier from the terminus position in 2021 (thick orange line in Fig. 1). This section was kept fixed in time and corresponded to 28 to 32 km for Glaciar O'Higgins, 69 to 73 km for Glaciar Viedma, 47 to 51 km for Glaciar Upsala, and 31 to 35 km for Glaciar Tyndall (thick orange line in Fig. 1).

3.3 Height above buoyancy near the ice front

We calculate the flotation height, h_f, when overburden ice pressure equals buoyancy force, using bed and ice surface topography maps: $h_f = h_b + (\rho_w/\rho_i)(h_w - h_b)$, where h_b is bed elevation and h_w is the elevation of water surface (Fig. 3). We assumed densities of 913 and 1,000 kg m^{-3} for ice (ρ_i) and lakewater (ρ_w), respectively. The equation suggests that a glacier flowing into deep water has a higher flotation height than a glacier which flows into shallow water. Thus, the minimum thickness above the flotation height is smaller for a glacier that flows into deep water than for a glacier flowing into shallow water if we assume the same ice cliff height above the water level. The height above buoyancy (h_{ab}) was defined by subtracting ice surface elevation (h_{DEM}) from flotation height to infer the floating condition near the ice front: $h_{ab} = h_{DEM} - h_f$. We defined a negative value of h_{ab} as a super-buoyant condition, while a positive value of h_{ab} is a grounded condition (Fig. 3). The uncertainty in the surface and bed elevation map was estimated to be 5.7 and 11 m, which results in an uncertainty of 14 m on average for the calculated floating condition.

4. Results

4.1 Lake bathymetry

4.1.1 Lago O'Higgins

The highest water depth in Lago O'Higgins was measured approximately at 41 km along the centreline with 799 m (Fig. 4a), which is similar to that reported by Schaefer and others (2011). From the deepest part, the water depth gradually decreased to 430 m at 35 km of the centreline, where the lake topography narrows (Fig. 2e). The water depth increases again by
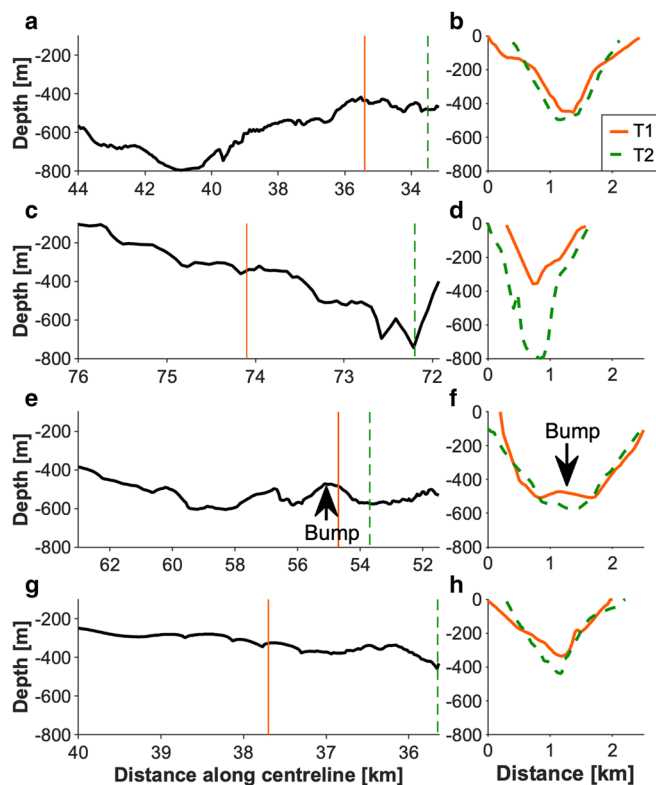
Figure 4. Longitudinal and cross-sectional profiles of (a) and (b) Lago O'Higgins, (c) and (d) Lago Viedma, (e) and (f) Brazo Upsala, and (g) and (h) Lago Geike. The right end of the profiles is the closest location to the glacier front with recorded depth data. Profiles T1 (solid orange line) and T2 (dashed green line), also indicated in the left panels by vertical lines, refer to the shallowest and the deepest sections of the lake, which were uncovered due to the glacier retreat over the last few decades. The longitudinal and cross-sectional profiles are indicated in Figure 2. The shallow bump detected in Brazo Upsala is indicated with black arrow.

60 m towards the glacier front and the deeper part is wider along the valley (Fig. 4a).

4.1.2 Lago viedma
The water depth increased along the centreline towards the glacier (Fig. 4c). The deepest part of the lake was ~750 m deep at 72.5 km on the centreline. The deeper part is also wider. For example, the width of the lake is about 1.3 km at the 74 km point along the centreline, increasing to 2 km at the 75 km point (Fig. 2f).

Although it is outside of our region of study, we observed a subaqueous moraine approximately 7 km from the current glacier front, which relates to a terminal moraine visible on the lake coastline (Fig. 2f). The peak of the morainal bank was observed at 5 to 180 m deep in the lake, which is surrounded by deeper and flatter basins (Fig. 2f). The subaqueous moraine is probably generated by the Little Ice Age glacier advance (Glasser and others, 2011), but not dated yet.

4.1.3 Brazo Upsala
Along Brazo Upsala, we observed the widest and one of the deepest U-shaped topographies within the region, which appeared after the glacier's retreat in 2000 (Figs 2g and 4f). A lake depth of more than 400 m is observed over 11 km from 62.5 km of the centreline towards the glacier (Figs 2g and 4e). The deepest part of the lake with a depth of 607 m was found at 58 km of the centreline. At 55 km of the centreline, a basal bump is observed, which is 100 m shallower than the surrounding lake. After the bump, the water depth increased by 100 m (to 570 m depth) at 54 km of the centreline. The water depth gradually decreased by 40–50 m towards the glacier (Fig. 2g).

4.1.4 Lago Geike
Lago Geike was the shallowest lake among those surveyed lakes. Along the centreline, the water depth increased towards the glacier from 245 m at 40 km to 350 m depth at 36 km (Fig. 2h). The maximum depth of 443 m was observed at the survey profile closest to the glacier (Fig. 4g).

4.2 Variations in ice-front position, ice speed, surface elevation, surface slope and height above buoyancy

4.2.1 Glaciar O'Higgins
Glaciar O'Higgins showed a substantial stepwise retreat since 2017 after about 15 years of stable ice-front position at 35 km on the centreline where shallow and narrow lake topography was observed (Figs 5a and b). In 2017, the ice front retreated by 600 m on average in the southern part (Fig. 5b). The ice front had been relatively stable until early 2019 after the retreat in 2017. Then the northern part of the ice front retreated by another 600 m on average (Fig. 5b). The ice front stabilized for two years until early 2021, but it started retreating in early 2021 and showed rapid retreat in October 2021. As the glacier retreated, the ice flow speed accelerated, and the lowering of the surface elevation was observed from the terminus to approximately 20 km upglacier.

Figure 6 shows temporal variations in ice-front position, surface speed, surface elevation and surface slope between 2000 and 2022. As the ice-front retreated stepwise since 2017, ice flow speed accelerated synchronously (Fig. 6a), implying a substantial increase in the frontal ablation rate. The ice flow speed was 2.0 km a^{-1} in the beginning of 2016, which increased slightly until the end of 2016 by 0.3 km a^{-1} (Figs 6a and 13). In January 2017, as the ice front retreated, the ice flow sped up substantially to 3.8 km a^{-1} (Fig. 6a). Another ice front retreat was observed in January 2019, accompanied by ice flow acceleration up to 4.2 km a^{-1} (Figs 6a and 13). In early 2022, it further increased from 3.5 km a^{-1} to 5.4 km a^{-1} (Fig. 6a). The mean elevation lowering rate was calculated between 28 and 32 km along the centreline (Fig. 6b). It showed 17.6 m a^{-1} between 2017 and 2022, which is 11 times greater than that observed between 2000 and 2015 (1.6 m a^{-1}) (Fig. 6b). The surface slope steepened during the rapid retreat after 2016 (Figs 6b and 14a). Between 2017 and 2022, the slope increased up to 6.2°, which was about 4.4° between 2000 and 2015 (Fig. 6b). The water depth at the ice-front position along the centreline shows that the ice front stayed slightly deeper in the water since 2016 (Fig. 6c), but still touched the bank opposed to the ice flow (Figs 5b and 6d). During the rapid retreat in 2017, water depth increased by 20 m, and the ice front detached from the bank (Figs 5b and 6d). The water depth at the centreline of the ice front decreased by about 20 m during late 2017 and 2018 (Fig. 6c) and then the ice front became relatively stable (Fig. 6a). Since January 2019, the water depth increased again by 20 m because of the rapid retreat. While the further retreat was observed in 2021, the lake topography is not covered by our measurements (Fig. 5b).

Figures 6d and e show the ice-front position, bed topography and the calculated height above buoyancy by assuming hydrostatic equilibrium in January 2005, April 2014, March 2016 and April 2018. In January 2005 and April 2014 the low value of the height above buoyancy indicates that the middle of the ice front is very close to floating condition, suggesting that ice front is still grounded (Figs 6e and 14a). However, it shows ~10 m below the flotation level on both sides of the ice front when the glacier slightly accelerated (Fig. 6a), while retreating rapidly in early 2017 (Figs 6a, d and e). The ice-front position was located at a similar place in 2018. Although our bathymetry covers only a part of the DEM, it shows the ice front is ~20 m below the
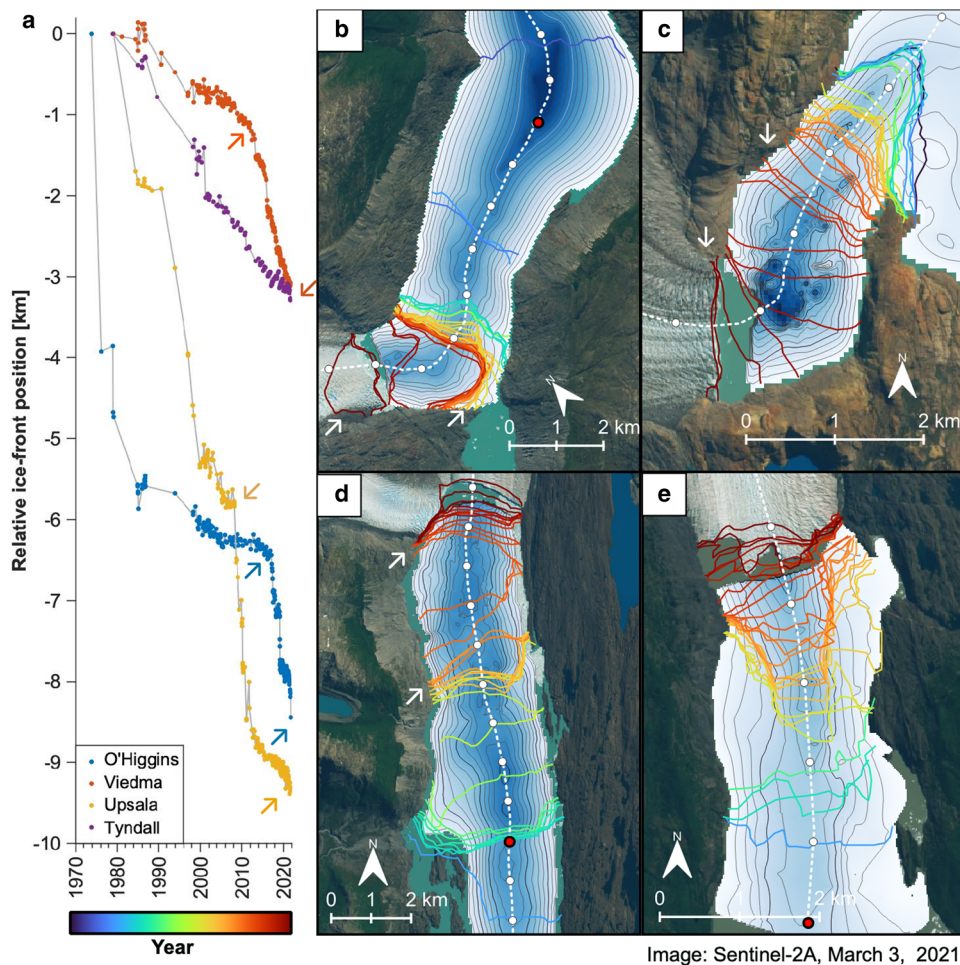
Figure 5. (a) Relative ice-front position change of the studied glaciers. Ice-front positions of (b) O'Higgins, (c) Viedma, (d) Upsala and (e) Tyndall glaciers. The colour of the ice front represents the date of the analysed image. The white arrows highlight the rapid retreat observed at O'Higgins, Viedma and Upsala glaciers. The white dashed line was used to interpolate the ice-front position to calculate the relative ice-front position change. The distance of the centreline is indicated by white and red circles every 1 and 10 km, respectively.

flotation level in April 2018 (Figs. 6e and 14a). This part retreated in early 2019 (Figs. 6a, d and e).

4.2.2 Glaciar Viedma

The rate of retreat for Glaciar Viedma has gradually increased (Figs. 5a and 7a). It was 33 m a^{-1} between 2000 and 2012 and increased to 200 m a^{-1} between 2012 and 2021, punctuated by relatively large retreats in April 2013 and February 2016 (Fig. 7a, highlighted by green squares). While ice speed did not show a substantial change before 2014, the surface ice speed (~0.6 km a^{-1}) starts to gradually accelerate after 2015 and reached a peak speed of 1.3 km a^{-1} in 2019 (Fig. 7a). Then, it showed a slight decrease towards 2021 (1.1 km a^{-1}) with clear seasonality (Fig. 7a). The surface elevation showed a larger lowering rate between 2012 and 2022 (12.4 m a^{-1}) than between 2000 and 2012 (5.0 m a^{-1}) while the surface slope increased from around 1.8° to around 2.4° between 2012 and 2018 (Fig. 7b). The retreat, acceleration, thinning and steepening is coincident with an ice-front retreat into the deep water (Fig. 7c). The water depth increased from 420 m to 510 m due to the retreat in April 2013. Until March 2016, the ice front was stable at that depth but retreated further into deeper water around 700 m, when the width of the ice front also showed the greatest value (Fig. 5c).

The floating level was calculated by using the surface and bed topographies in February 2012, February 2013, December 2015

and October 2016 (Figs 7e and 14b). While the glacier height was above flotation level in February 2012, it was below flotation level at the middle part of the ice front in February 2013 (Fig. 7e), coincident with the ice front's retreat into deep water (Fig. 7c). One of the largest retreats was observed at the beginning of 2016. The height above buoyancy calculated in December 2015 shows that the north-eastern part of the ice front was 10 to 20 m below zero (Fig. 7e). In October 2016, the middle part of the ice front showed a negative height above buoyancy, after which the ice front retreated over the deepest part of the lake (Fig. 14b).

4.2.3 Glaciar Upsala

The rapid ice front retreat initiated in 2008 was accompanied by ice flow acceleration and thinning, which have been reported by previous studies (Sakakibara and others, 2013; Sakakibara and Sugiyama, 2014). In addition to their findings, we found that the ice speed and slope have gradually increased since 2005 (Figs. 8a and b). The rapid retreat and acceleration were initiated in 2008 (Fig. 8), when the ice front detached from the bedrock bump at 8 km of the centreline (Figs. 2g and 8d). During the rapid retreat between 2008 and 2011, the surface slope also increases at a rate of 0.24° a^{-1} (Fig. 8b). The mean surface lowering rate calculated between 2008 and 2012 was 29.5 m a^{-1}, which is close to three times larger than that calculated between 2000 and 2021 (11.8 m a^{-1}).
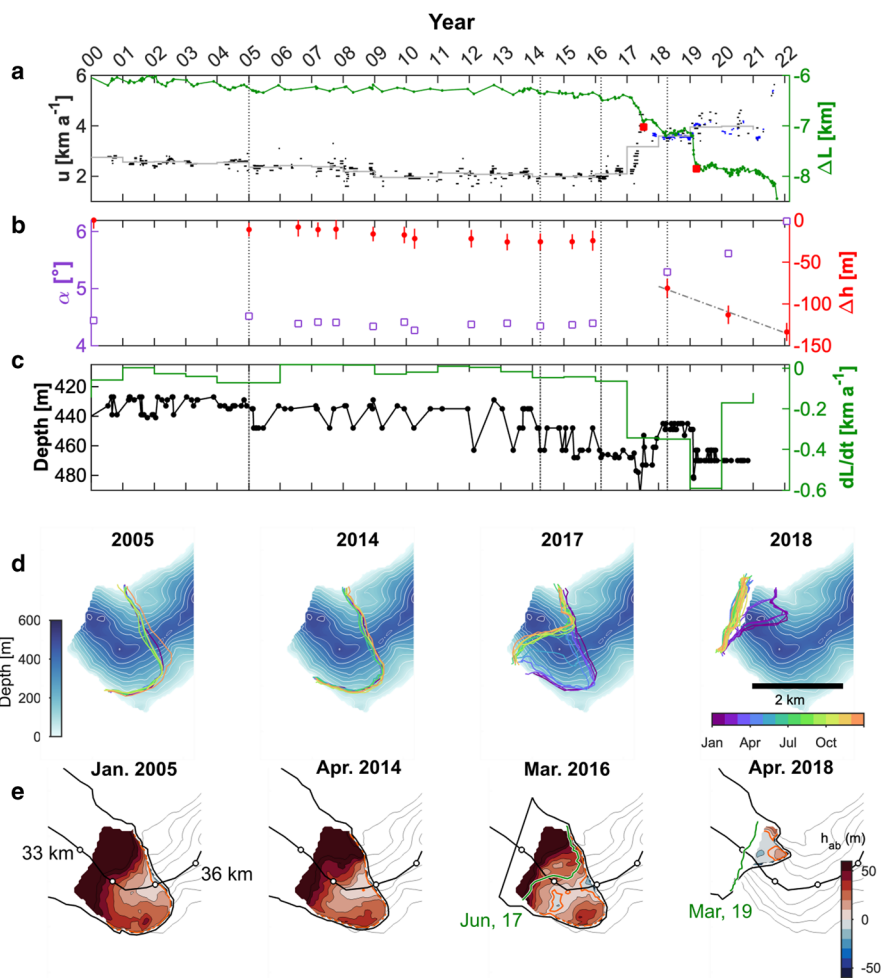
Figure 6. (a) Time-series of ice speed (black and blue dots) and ice front position (green dots) for Glaciar O'Higgins. The grey line indicates annually averaged surface ice speed, weighted for temporal separations. Figure 13 shows the variables between 2014 and 2018. (b) Ice surface elevation (red dots) and surface slope (purple square). The dot-dash line is the best-fit linear regression line for the elevation change based on three DEMs between 2018 and 2022. (c) Water depth at the calving front along the centreline (black dots) and terminus position change rate (green line). Because our bathymetry data has limited coverage near the ice front, there are data gaps in the water depth in recent years. (d) Ice-front positions and lake topographies. Ice-front positions analysed in 2005, 2014, 2017 and 2018 are indicated in each panel with a colour code. (e) Height above buoyancy was calculated from surface elevation and bathymetry map of the glacier with an average error of ±14 m. The timing of the calculation is indicated by a black dot line in panels (a)–(d). The orange line highlights where the height above buoyancy is zero. Green lines indicate the retreated ice-front position after the floating condition, which is also indicated by the red square in panel (a). The longitudinal profile of the ice surface elevation along the centreline is depicted in Fig. 14a.

The calculated height above buoyancy using surface elevation and bed topography shows that the ice front was well below the flotation level before the rapid retreat event occurred (Figs. 8d, e and 14c). Intriguingly, in the case of Glaciar Upsala, the retreated ice front appears to follow the contour line where height above buoyancy becomes zero (Fig. 8e). In February 2005, half of the eastern ice front was about 10 m below the floating condition and retreated in April 2005 as indicated by the green line (Fig. 8e). In February 2008, the terminus over the bedrock bump was above the flotation level, but it was 10 to 20 m below the flotation level 1 to 2 km up-glacier from the ice front, which retreated by May 2009 (Fig. 8e). Another calculation of the height above buoyancy in January 2009 suggests that while the ice front is located over the bump, the glacier height is well below the flotation level, suggesting no buttressing from the bedrock bump (Figs. 8e and 14c). When the ice speed, thinning rate and surface slope showed their maximum between the end of 2009 and the beginning of 2010, most parts of the ice front up to 2 km up-glacier was 20 m below the flotation level (Figs. 8e and 14c). A satellite image from December 2009 indicates that the margins of the lower part of the glacier were highly fractured and a marginal rift propagated from the western margin (Fig. 15a). The glacier front had calved off by May 2010 and generated tabular icebergs (Fig. 15b).

4.2.4 Glaciar Tyndall

Glaciar Tyndall has retreated almost at a near constant rate between 2000 and 2021 (79.6 m a^{-1}), but the retreat was characterized by large episodic tabular iceberg calving events (Fig. 5a and 9a), observed in 2001 and 2010 (Figs. 15c, d). During the

mid-2000, the ice front of Glaciar Tyndall developed a formation of long, narrow tongues (Fig. 5e). Dense mapping of the ice-front position since 2016 indicates that the ice front continuously advances for one to two years followed by occasional retreat by calving in the summer (Fig. 9a). There is no clear interannual variability in surface ice speed and surface slope (Figs. 9a and b). The surface elevation was lowered by 153 m between 2000 and 2021 (Fig. 9b). Water depth was similar for the ice front between 2000 and 2010, while the ice front width narrowed by 200 m during the same period (Fig. 9c). Since 2010 the water depth gradually increased from 380 m to 420 m (Fig. 9c).

Height above buoyancy calculations suggested that the ice front of Glaciar Tyndall was in near- or super-buoyant conditions in 2000, 2005 and 2010 (Figs. 9e and 14d), where we have DEM overlapped with the lakebed topography (Fig. 9d). A relatively large retreat was observed in 2001 and 2010, where most of the ice front was 10 m below floating condition, calculated in February 2000 and July 2011 (Fig. 9e).

5. Discussion

We measured the detailed lake topography near the ice fronts of O'Higgins, Viedma, Upsala and Tyndall glaciers (Fig. 2). The resulting bathymetries show close relation with glacier's retreat, acceleration and thinning (Figs 6–9). The bathymetric data can be utilized to improve the estimation of ice discharge from the selected glaciers (Minowa and others, 2021), as well as for calibration and validation of ice thickness inversion methods (e.g. Morlighem and others, 2011; Fürst and others, 2017). In this
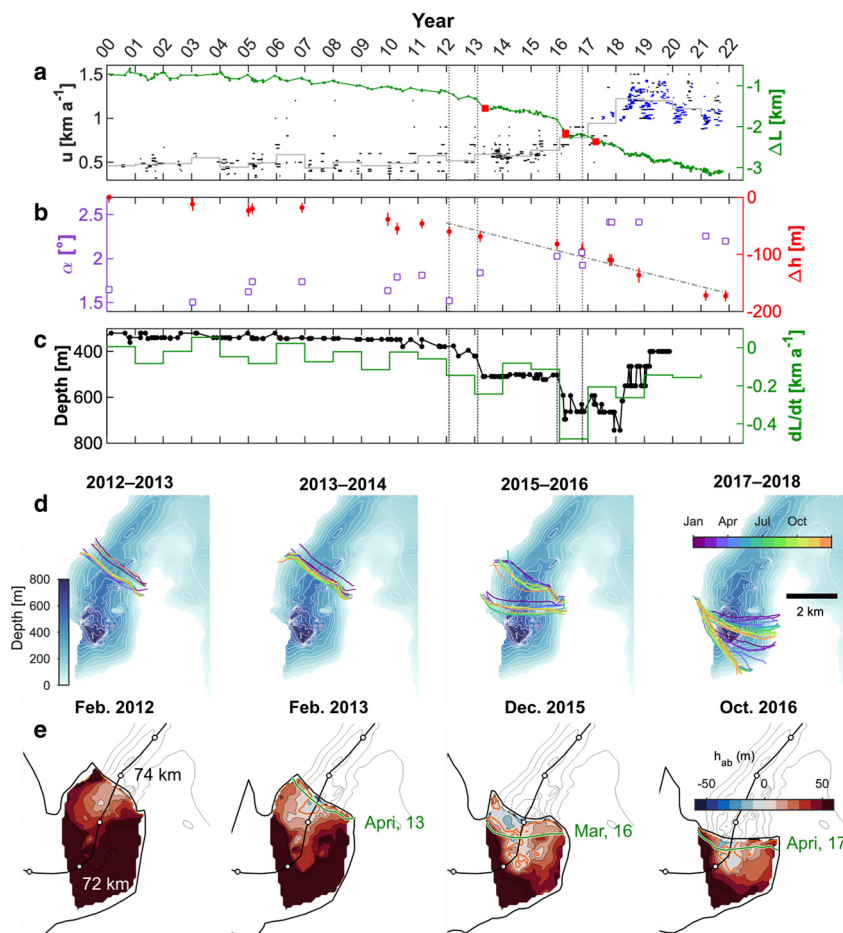
Figure 7. Similar plots as in Figure 6 for Glaciar Viedma. (d) Note that two years of ice-front positions are indicated.

study, we utilize the data to investigate observed glacier dynamics and discuss possible mechanisms of rapid changes in ice flow, glacier calving and ice-front position. We also discuss the difference between lake-terminating glaciers in Patagonia and calving glaciers in other regions of the world.

5.1 Importance of a super-buoyant ice front for the rapid glacier mass loss

Comparison of bedrock topography with ice-front position and ice speed shows that lake topography controls the rapid retreat observed at O'Higgins, Viedma and Upsala glaciers (Figs 6–9). We observed gradual ice speed acceleration at Glaciar O'Higgins in 2016 prior to its rapid retreat and acceleration (Figs 6 and 13). Noisier but similar gradual ice speed acceleration was observed at Glaciar Upsala since 2005 prior to its rapid retreat in 2008 (Fig. 8a) as reported by Sakakibara and others (2013). At Glaciar Viedma, ice flow gradually increased for multiple years since 2012 (Fig. 7a). The calculation of flotation level suggests that the ice front was in a super-buoyant condition, and that also further upstream the glacier was near buoyant condition during the gradual flow acceleration of those glaciers (Figs. 6e, 7e, 8e and 14). These results suggest that the effective pressure decreased by losing overburden ice pressure and parts of the ice front decoupled from the bed, resulting in an increase of basal sliding near the ice front.

After the gradual ice flow acceleration, rapid glacier retreat and acceleration were observed coincident with ice front retreat from different pinning points: the opposed bank at Glaciar O'Higgins (Fig. 5b), the bedrock bump at Glaciar Upsala (Fig. 5d) and

shallow and narrow topography at Glaciar Viedma (Fig. 5c). A comparison of the ice-front position and height above buoyancy shows that the ice-front retreated approximately along the contour line of the height above buoyancy equals zero (Figs. 6e–9e). This implies that a buoyancy force acts on the terminus, and can cause it to develop basal crevasses through a concentration of large basal tensile stresses and eventually triggers a large-scale and full-thickness iceberg calving event (e.g. Parizek and others, 2019; Trevers and others, 2019). The rapid flow acceleration followed by ice front detachment from the pinning point suggests that a sudden change in the force balance due to a strong reduction in basal friction caused substantial ice flow acceleration (O'Neel and others, 2005; Howat and others, 2007). On the other hand, a more gradual acceleration was observed in Glaciar Viedma, which has narrower lake bedrock topography than Glaciar O'Higgins and Glaciar Upsala (Figs. 2 and 4). Glaciar Tyndall did not show any flow acceleration even after the glacier retreated into deeper water (Figs. 9 and 14d). These differences might indicate that lateral shear stress makes an important contribution to the force balance near the front of Viedma and Tyndall glaciers due to narrower lake topography (Fig. 4). Viedma and Tyndall glaciers have lower flow speed than Upsala and O'Higgins glaciers, resulting in lower stresses to fracture ice. This idea seems to be plausible, as we observe less crevasses in satellite images and in the field in Viedma and Tyndall glaciers. Less fractured ice for those glaciers may have more resistance to the buoyancy force.

The substantial flow acceleration is accompanied by an increase in glacier calving and therefore ice front retreat in O'Higgins, Viedma and Upsala glaciers (Figs 6–8). Our results indicate that super-buoyant conditions play an important role
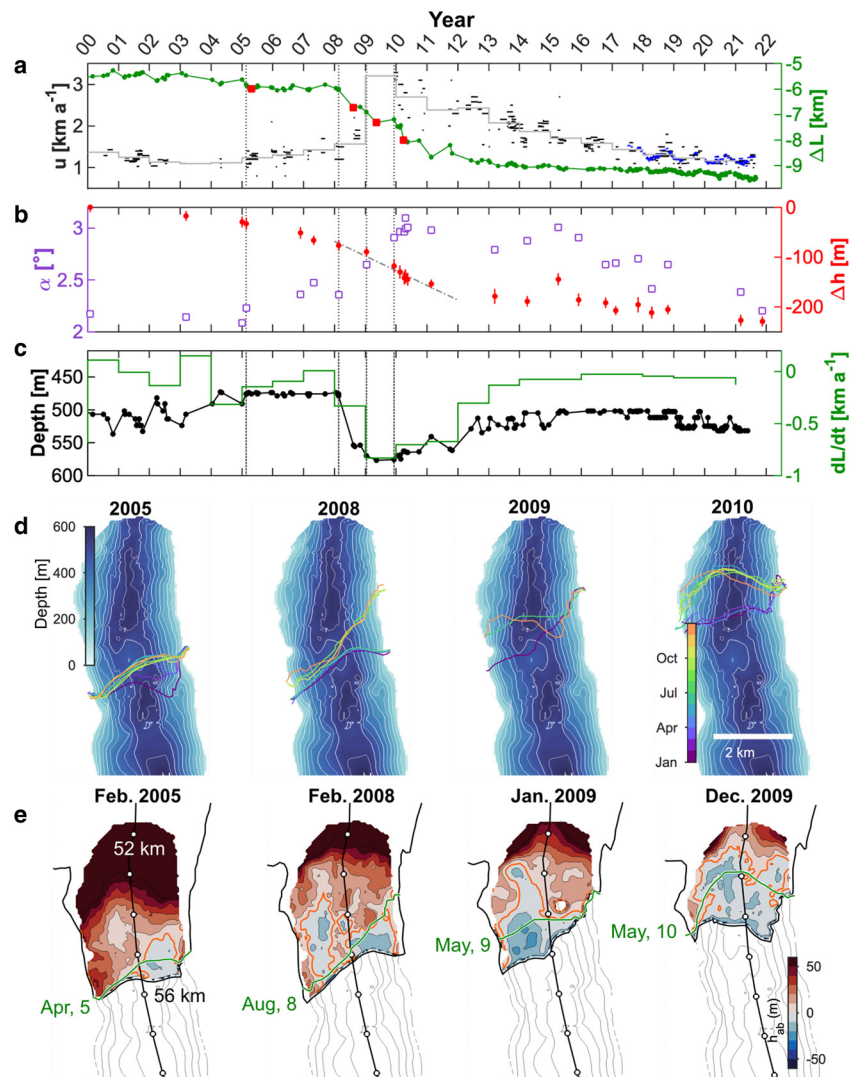
Figure 8. Similar plots as in Fig. 6 for Glaciar Upsala. (e) Note that the bedrock bump was observed at 55 km along the centreline.

in calving and retreat. The short-lived floating condition is supported by the tabular icebergs observed in front of Glaciar Upsala during the rapid retreat between 2008 and 2011 (Fig. 15b). Two tabular icebergs, with approximate dimensions of 600×500 m and 300×800 m, float in Brazo Upsala (Fig. 15b). Our height above buoyancy calculation indicated that these icebergs were generated from the region where more than 2 km of the ice front was in a floating condition (Figs. 8e and 14c). In addition to increased fracturing due to the acceleration of ice flow, the buoyancy force might generate a full-thickness crevasse from the base of the glacier (Parizek and others, 2019; Trevers and others, 2019), resulting in tabular icebergs and rapid retreat (e.g. van der Veen, 2002; Benn and others, 2007). Previous studies found that increased ice flow, high water pressure at the grounding line and buoyancy torque favour the development of basal crevasses (van der Veen, 1998; Nick and others, 2010). We did not observe any similar tabular icebergs in front of O'Higgins and Viedma glaciers and the height above buoyancy calculation suggests that the floating part is relatively limited when compa
red with that observed in front of Glaciar Upsala (Figs. 6e and 7e). Whether an iceberg capsizes or not is determined by the aspect ratio of the iceberg's width and thickness (Burton and others, 2012). The limited region of the floating portion suggests that even though there is full-thickness calving, the iceberg capsizes and breaks off into pieces. These type of floating conditions near a glacier front was suggested to exist at ocean-terminating

glaciers (Howat and others, 2005, 2007, 2008; Joughin and others, 2008).

In contrast, we observed a near flotation ice front for three available DEMs between 2000 and 2010 at Glaciar Tyndall without observing acceleration and rapid retreat (Fig. 9). At Glaciar Tyndall, we also observed tabular icebergs in 2005 and 2017 with dimensions similar to those observed in front of Glaciar Upsala (Figs. 15c and d). Compared with the other three glaciers, Glaciar Tyndall has a much lower flow speed ($\sim$500 m a^{-1}) and flows into a shallower lake (300 to 400 m). We speculate that due to the lower flow speed of the glacier, it might have less fractured ice and that the buoyancy for this glacier might result in the formation of a floating tongue.

While our analyses suggest the importance of an ungrounded ice front in flow acceleration and large-scale calving at lake-terminating glaciers, our floating-level calculation is limited in time. Analysing floating conditions and ice flow more frequently will eventually improve our understanding of the cause of flow acceleration and iceberg calving. If the bedrock topography is known, these analyses can be accomplished by oblique photogrammetry (James and others, 2014; Murray and others, 2015) or terrestrial radar interferometry (Parizek and others, 2019; Walter and others, 2020; Cook and others, 2021). However, such field observations are usually conducted in the summer months. Capturing the whole process of the rapid retreat is still challenging and can take several years in the case of Patagonian glaciers.
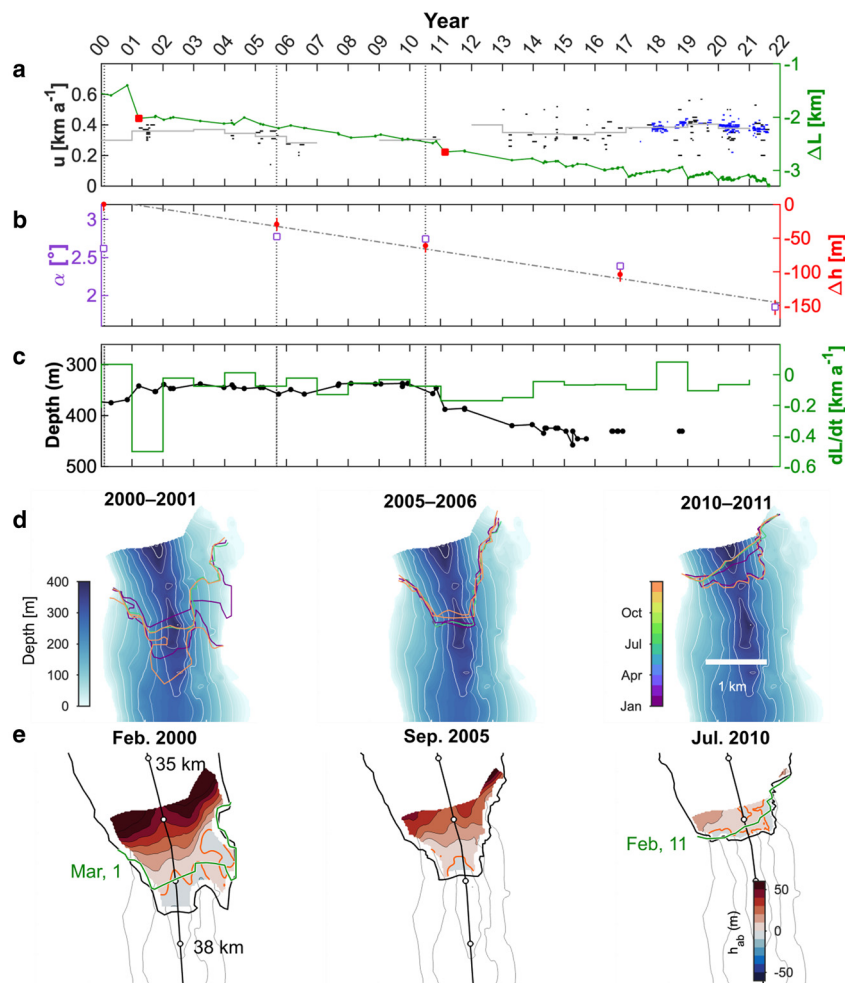
Figure 9. Similar plots as in Fig. 6 for Glaciar Tyndall. (d) Note that two years of ice-front positions are indicated.

5.2 Rapid retreat of Glaciar Upsala

Of the glaciers in this study, the ice front retreat and acceleration were the strongest at Glaciar Upsala, resulting in the formation of marginal rifts and calving of tabular icebergs (Figs. 6–9 and 15). Longitudinal and shear strain rates were calculated based on the satellite-derived velocities before and after the event at Glaciar Upsala (Fig. 10). The strain rate tensor is calculated by spatially differentiating the velocity field in initially Universal Transverse Mercator coordinates system and rotated with ice flow direction (e.g. Stearns and others, 2015). Two velocity fields were used to calculate strain rates between 28th September and 14th October in 2001, and between 14th and 30th August in 2008. In both cases, the velocity was determined over the entire region near the ice front (Figs. 10a and d). Uncertainties in the calculated strain rates originating from the errors in the velocity fields were $0.5\ a^{-1}$ for 2001 and $0.8\ a^{-1}$ for 2008 on average.

The flow speed increased all over the lower part of the glacier terminus in 2008 in comparison to 2001 (Figs. 10a, d and g), and was particularly enhanced over the western part of the terminus up to $1\ km\ a^{-1}$ (Fig. 10g). The strongly accelerated part appears to be coincident with the place where the glacier floated as inferred from the height above buoyancy calculation (orange line in Figs. 10d and g). Most notably, the shear strain rate over the western margin in the lower part of the glacier varied between 2001 and 2008 (Figs. 10c, f and i). The substantial flow acceleration due to the decoupling of ice from the base caused contrasting flow speed differences between the margin and central part of the ice flow, which enhanced the shear strain rate in that region. Interestingly, the marginal rift observed on December 2009 was

developed over the western margin, where high ice fracture is expected due to the high shear strain rates (Figs. 10i and 15a). Similar rift development and propagation into fast flow are often observed on ice shelves in Antarctica (e.g. Alley and others, 2019; Benn, 2022) and Greenland (e.g. Falkner and others, 2011), due to strong flow speed contrast between marginal and central parts of the ice shelf. To our knowledge, this process has never been reported for lake-terminating glaciers. The strong flow acceleration due to the transient floating tongue and overdeepening may be the cause of this rare calving event observed at Glaciar Upsala (Fig. 15b).

5.3 Comparison of Patagonian lake-terminating glaciers with calving glaciers in other regions

Because the ice flow, calving and changes in ice-front position are closely related to water depth near the terminus of calving glaciers, we compared width-averaged water depth and frontal ablation rate among the calving glaciers in Patagonia (Warren and others, 1995a, 1995b; Warren and Aniya, 1999; Rignot and others, 1996; Rivera and others, 1997; Rott and others, 1998), Alaska (Brown and others, 1982; Meier and others, 1985; Funk and Röthlisberger, 1989; Pelto and Warren, 1991; Motyka and others, 2003), Greenland (Funk and Röthlisberger, 1989; Pelto and others, 1989; Pelto and Warren, 1991), New Zealand (Hochstein and others, 1995; Warren and Kirkbride, 2003), Alps (Funk and Röthlisberger, 1989), Iceland (Björnsson and others, 2001), Norway (Laumann and Wold, 1992) and Svalbard (Pelto and Warren, 1991) (Fig. 11 and supplementary dataset).
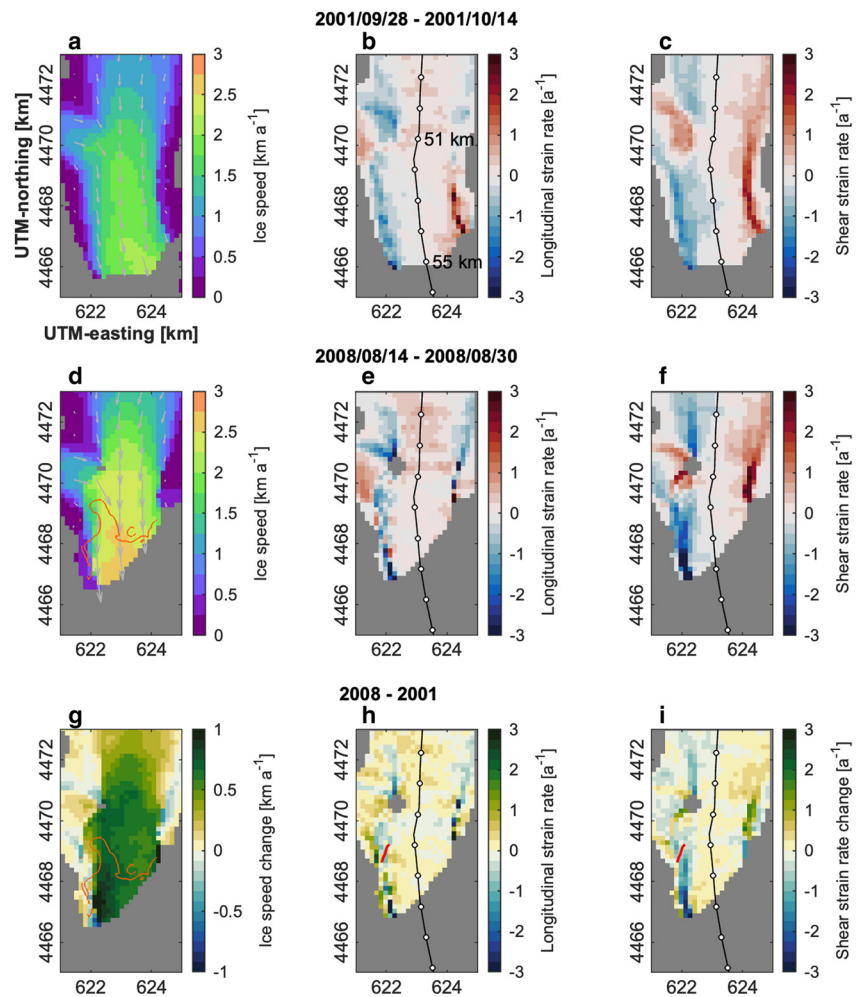
Figure 10. (a) Surface ice speed, (b) longitudinal strain rate and (c) shear strain rate calculated between 28th September and 14th October 2001 in Glaciar Upsala. Grey arrows show flow direction. (d)–(f) Calculated between 14th and 30th August 2008, when the glacier showed acceleration and rapid ice-front retreat (Fig. 8). (d) The orange line indicates the place where the height above buoyancy becomes zero calculated with ASTER DEM of January 2009 (Fig. 8e). (g) Changes in surface ice speed, (h) longitudinal strain rate and (i) shear strain rate were calculated by subtracting the 2008 data from the 2001 data. (h) and (i) The marginal rift observed on the satellite image of December 2009 is indicated by a red line. The centreline of the glacier is shown by white circles, dotted every 1 km. At 55 km of the centreline, a bump was observed in the lake topography (Fig. 2g).

Width-averaged frontal ablation rate a (sum of iceberg calving and subaqueous ice cliff melting) was estimated by subtracting the width-averaged ice speed near the terminus (u_m) with the change of ice-front position (dL/dt): $a = u_m - dL/dt$. We used annual mean ice speed and mean change of ice-front position in 2001 to calculate the frontal ablation rate because of the abundant availability of ice-front position, surface speed and water depth data to calculate annual mean frontal ablation rate (Supplementary dataset). In addition to this, both the ice speed and the change of ice-front position vary strongly during the dynamic glacier retreat (Figs. 6–9). Thus, the frontal ablation rate was calculated in 2001 to avoid such influences when comparing with other glaciers. Width-averaged water depth was obtained from cross-sectional profiles based on the observed water depth, set close to the ice front in 2001.

Compared to lake-terminating glaciers in other regions, the Patagonian glaciers terminate in much deeper lakes ranging between 100 and 500 m and experience higher frontal ablation rates (Fig. 11a). The deep lakes in Patagonia appear to be developed by a high glacial erosion rate due to a warm climate, abounded subglacial discharge and high basal sliding (Koppes and others, 2015). The great depth near the glacier terminus causes greater flow in the Patagonian glaciers compared to the calving glaciers in other regions, resulting in larger frontal ablation. It may also explain the greater retreat and thinning rates at O'Higgins, Upsala and Viedma glaciers compared to lake-terminating glaciers in Alaska (Boyce and others, 2007; Trüssel and others, 2013), the Alps (Tsutaki and others, 2013) and Himalaya (Sato and others, 2022). The accelerated flow, thinning

rate and retreat rate reached 1–6 km a^{-1}, 10–50 m a^{-1} and 0.4–0.8 km a^{-1}, respectively, for those three glaciers in Patagonia, while these numbers were one to two orders of magnitude smaller in the lake-terminating glaciers in the other regions (Boyce and others, 2007; Tsutaki and others, 2013; Trüssel and others, 2013; Sato and others, 2022). We expect there are several factors causing this difference: Patagonian lake-terminating glaciers are relatively thick, experience high surface slopes and flow into wide and deep lakes, resulting in higher driving stress and ice speed. In such conditions, the increase in the ice speed near the terminus of the glaciers in Patagonia can result in a greater magnitude of the dynamic thinning than the calving glaciers in other regions.

Lake-terminating glaciers are usually expected to experience lower frontal ablation rates compared to ocean-terminating glaciers, which is also supported by our study (Fig. 11b). In particular, a clear contrast can be found between the lake-terminating glaciers in Patagonia and the ocean-terminating glaciers in Alaska, both located in similar maritime climate settings. The frontal ablation estimated for Glaciar San Rafael in Patagonia, which flows into a brackish water, is in line with those reported for ocean-terminating glaciers in Alaska (Fig. 11b). Lake-terminating glaciers in Patagonia have contrasting processes occurring at their front compared to ocean-terminating glaciers due to the difference of water density in front of the glaciers (Sugiyama and others, 2016; Truffer and Motyka, 2016). The fresh and turbid subglacial water discharge into the fjords generates an upwelling plume, which effectively entrains the warm deep water to melt the ice under the water
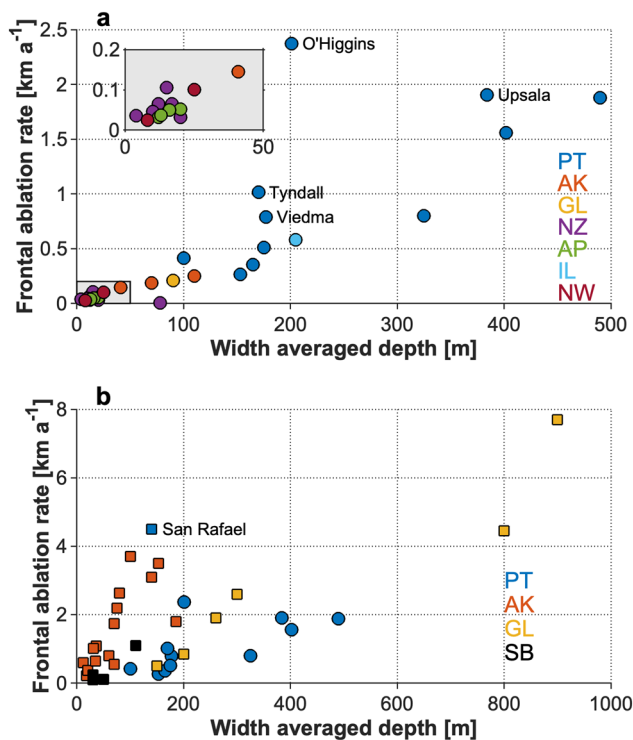
Figure 11. (a) Comparison between width-averaged water depth and frontal ablation rate for lake-terminating glaciers. Colour of the markers indicates the region of the lake-terminating glaciers: PT–Patagonia, AK–Alaska, GL–Greenland, NZ–New Zealand, AP–Alps, IL–Iceland and NW–Norway. Inset shows an enlarged plot of water depth against frontal ablation rate for shallow water glaciers less than 50 m deep. (b) A similar plot for lake-terminating glaciers in Patagonia (PT) is indicated by circles and ocean-terminating glaciers in Alaska (AK), Greenland (GL) and Svalbard (SB) are indicated by squares. Dataset sources are summarized in the supplementary dataset.

(e.g. Motyka and others, 2003, 2013). In contrast, the subglacial discharge normally stays deep in freshwater lakes and limits subaqueous melting (Sugiyama and others, 2016, 2021; Minowa and others, 2017). Active submarine melting may destabilize the subaerial part of the calving front and enhance glacier calving for the ocean-terminating glaciers. The limited amount of subaqueous melting in the lakes favours keel development, which may in the end cause buoyancy-driven large-scale calving (Purdie and others, 2016; Sugiyama and others, 2019). Additionally, the water density difference causes a higher buoyancy force for ocean-terminating glaciers than for lake-terminating glaciers. van der Veen (2002) pointed out that effective pressure more substantially decreases when the ice front is close to flotation for an ocean-terminating glacier than for a lake-terminating glacier. These differences may result in greater ice front retreat, acceleration and thinning in ocean-terminating glaciers in Alaska (e.g. O'Neel and others, 2005; Pfeffer, 2007) and Greenland (e.g. Howat and others, 2005, 2007, 2008; Joughin and others, 2008; Catania and others, 2018).

Many calving glaciers have shown retreat and thinning over the last several decades in Patagonian icefields (e.g. Aniya and others, 1997; Rignot and others, 2003; Sakakibara and Sugiyama, 2014; Minowa and others, 2021). The dynamic retreat which accompanied flow acceleration was observed for several glaciers, which dominated the mass loss in the entire region (Minowa and others, 2021). Yet, bedrock topography is coarse, and coverage is especially limited in the lower ablation area, which is the most important place to interpret the fluctuation of outlet glaciers in Patagonia (Gourlet and others, 2016; Millan and others, 2019). Since these dynamic retreats are highly

sensitive to bedrock topography, further observations are strongly recommended to understand the fate of glaciers in Patagonia. Archiving such high-resolution topography datasets is still very challenging for gravity surveys due to the large spatial footprint. For ice radars, the measurements are challenging, particularly in lower parts of the glacier due to the influence of deep valleys, crevasses and the abundance of water in temperate ice (Zamora and others, 2009; Gourlet and others, 2016; Millan and others, 2019). Modelling studies on the future evolution of calving glaciers using these coarse topography maps should be aware of the uncertainties in bed topography.

6. Conclusions

We measured the lake topography near the terminus of O'Higgins, Viedma, Upsala and Tyndall glaciers in the southern Patagonian icefield, which terminate in freshwater lakes. Ice-front position, ice speed, surface elevation, and surface slope of these glaciers were analysed based on multiple optical remote sensing datasets over the last several decades and compared with lake topography. O'Higgins, Viedma and Upsala glaciers showed high sensitivity to changes in their near terminus geometry, while Glaciar Tyndall did not. We hypothesized that the less sensitive behaviour of Glaciar Tyndall is due to the shallower and narrower lake than other lakes resulted in less ice flow and less importance of the buoyancy force near the ice front.

A rapid retreat was observed at O'Higgins and Viedma glaciers from 2016 onwards, and at Glaciar Upsala between 2008 and 2011. Floating level calculation suggests that the overdeepening basins and long-term thinning has caused a transiently super-buoyant condition near the terminus. Ice flow gradually increased when the floating condition or super-buoyant condition was reached near the ice front. Basal sliding is probably enhanced due to the reduced effective pressure or loss of basal drag due to the decoupling of the ice front from the ground. Large ice-front retreat occurred over the regions where super-buoyant conditions were observed. Once the ice front detached from the pinning point due to buoyancy-driven iceberg calving, ice flow accelerates by losing resistance force from the bedrock, and the glacier thins substantially due to the dynamic thinning. Further studies are desirable that consider the influence of meteorological and/or limnological conditions on the surface lowering to understand the trigger of the sequence of the rapid glacier mass loss.

The lake-terminating glaciers in Patagonia flow into deeper lakes than lake-terminating glaciers in other regions, resulting in larger ice flow and frontal ablation and greater potential for dynamic ice mass loss. Yet, it is not clear whether the observed rapid mass loss in Patagonian icefields will continue, as there is a lack of a reliable high-resolution bedrock topography data. Further observations of bed geometry with ice radar and gravity measurements will certainly help to understand the fate of Patagonian glaciers. Numerical projections should consider the uncertainty associated with the very high sensitivity of glacier dynamics to bedrock geometry near the ice front.

References

Abdel Jaber W, Rott H, Floricioiu D, Wuite J and Miranda N (2019) Heterogeneous spatial and temporal pattern of surface elevation change and mass balance of the Patagonian ice fields between 2000 and 2016. *Cryosphere* **13**(9), 2511–2535. doi:10.5194/tc-13-2511-2019

Alley KE, Scambos TA, Alley RB and Holschuh N (2019) Troughs developed in ice-stream shear margins precondition ice shelves for ocean-driven breakup. *Science Advances* **5**(10), eaax2215. doi:10.1126/sciadv.aax2215

Amundson JM and 5 others (2008) Glacier, fjord, and seismic response to recent large calving events, Jakobshavn Isbræ, Greenland. *Geophysical Research Letters* **35**(22), 2–6. doi:10.1029/2008GL035281

Amundson JM, Truffer M and Zwinger T (2022) Tidewater glacier response to individual calving events. *Journal of Glaciology* **68**, 1117–1126. doi:10.1017/jog.2022.26

Aniya M, Sato H, Naruse R, Skvarca P and Casassa G (1997) Recent glacier variations in the Southern Patagonia Icefield, South America. *Arctic, Antarctic, and Alpine Research* **29**(1), 1–12. doi:10.2307/1551831

Benn DI and 10 others (2022) Rapid fragmentation of Thwaites Eastern Ice Shelf. *Cryosphere* **16**(6), 2545–2564. doi:10.5194/tc-16-2545-2022

Benn DI, Cowton T, Todd J and Luckman A (2017) Glacier calving in Greenland. *Current Climate Change Reports* **3**(4), 282–290. doi:10.1007/s40641-017-0070-1

Benn DI and Warren CR and Mottram RH (2007) Calving processes and the dynamics of calving glaciers. *Earth-Science Reviews* **82**(3-4), 143–179. doi:10.1016/j.earscirev.2007.02.002

Bevan SL, Luckman AJ and Murray T (2012) Glacier dynamics over the last quarter of a century at Helheim, Kangerdlugssuaq and 14 other major Greenland outlet glaciers. *Cryosphere* **6**(5), 923–937. doi:10.5194/tc-6-923-2012

Björnsson H, Pálsson F and Guðmundsson S (2001) Jökulsárlón at Breiðamerkursandur, Vatnajökull, Iceland: 20th century changes and future outlook. *Jökull* **50**, 1–18.

Boyce ES, Motyka RJ and Truffer M (2007) Flotation and retreat of a lake-calving terminus, Mendenhall Glacier, southeast Alaska, USA. *Journal of Glaciology* **53**(181), 211–224. doi:10.3189/172756507782202928

Brown CS and 5 others (1982) *Calving speed of Alaska tidewater glaciers, with application to Columbia Glacier*, Vol. **1258**, Washington: US Government Printing Office.

Burton JC and 9 others (2012) Laboratory investigations of iceberg capsize dynamics, energy dissipation and tsunamigenesis. *Journal of Geophysical Research: Earth* **117**(F1), F01007. doi: 10.1029/2011JF002055.

Casassa G, Brecher H, Rivera A and Aniya M (1997) A century-long recession record of Glaciar O'Higgins, Chilean Patagonia. *Annals of Glaciology* **24**, 106–110. doi:10.3189/S0260305500012015

Catania G and 7 others (2018) Geometric controls on tidewater glacier retreat in central western Greenland. *Journal of Geophysical Research: Earth* **123**(8), 2024–2038. doi:10.1029/2017JF004499

Christmann J and 10 others (2021) Elastic deformation plays a non-negligible role in Greenland's outlet glacier flow. *Communications Earth & Environment* **2**(1), 232.

Cook SJ, Christoffersen P, Truffer M, Chudley TR and Abellan A (2021) Calving of a large Greenlandic tidewater glacier has complex links to meltwater plumes and mélange. *Journal of Geophysical Research: Earth* **126**(4). e2020JF006051. doi:10.1029/2020JF006051

Cook SJ and Swift DA (2012) Subglacial basins: Their origin and importance in glacial systems and landscapes. *Earth-Science Reviews* **115**(4), 332–372. doi:10.1016/j.earscirev.2012.09.009

De Angelis H (2014) Hypsometry and sensitivity of the mass balance to changes in equilibrium-line altitude: the case of the Southern Patagonia Icefield. *Journal of Glaciology* **60**(219), 14–28. doi: 10.3189/2014JoG13J127

Doyle SH and 7 others (2018) Physical conditions of fast glacier flow: 1. Measurements from boreholes drilled to the bed of Store Glacier, West Greenland. *Journal of Geophysical Research. Earth Surface* **123**(2), 324–348. doi:10.1002/2017JF004529.

Enderlin EM and Howat IM (2013) Submarine melt rate estimates for floating termini of Greenland outlet glaciers (2000–2010). *Journal of Glaciology* **59**(213), 67–75. doi:10.3189/2013JoG12J049

Falkner KK and 10 others (2011) Context for the recent massive Petermann Glacier calving event. *Eos, Transactions American Geophysical Union* **92**(14), 117–118. doi:10.1029/2011EO140001

Felikson D and 11 others (2017) Inland thinning on the Greenland ice sheet controlled by outlet glacier geometry. *Nature Geoscience* **10**(5), 366–369. doi:10.1038/ngeo2934

Frank T, Åkesson H, de Fleurian B, Morlighem M and Nisancioglu KH (2022) Geometric controls of tidewater glacier dynamics. *Cryosphere* **16**(2), 581–601. doi:10.5194/tc-16-581-2022

Funk M and Röthlisberger H (1989) Forecasting the effects of a planned reservoir which will partially flood the tongue of Unteraargletscher in Switzerland. *Annals of Glaciology* **13**, 76–81. doi:10.3189/S0260305500007679

Fürst JJ and 14 others (2017) Application of a two-step approach for mapping ice thickness to various glacier types on Svalbard. *Cryosphere* **11**, 2003–2032. doi:10.5194/tc-2017-30

Glasser NF, Harrison S, Jansson KN, Anderson K and Cowley A (2011) Global sea-level contribution from the Patagonian Icefields since the Little Ice Age maximum. *Nature Geoscience* **4**(5), 303–307. doi:10.1038/ngeo1122

Gourlet P, Rignot E, Rivera A and Casassa G (2016) Ice thickness of the northern half of the Patagonia Icefields of South America from high-resolution airborne gravity surveys. *Geophysical Research Letters* **43**(1), 241–249. doi:10.1002/2015GL066728

Haug T, Kääb A and Skvarca P (2010) Monitoring ice shelf velocities from repeat MODIS and Landsat data–a method study on the Larsen C ice shelf, Antarctic Peninsula, and 10 other ice shelves around Antarctica. *Cryosphere* **4**(2), 161–178. doi:10.5194/tc-4-161-2010

Heid T and Kääb A (2012) Evaluation of existing image matching methods for deriving glacier surface displacements globally from optical satellite imagery. *Remote Sensing of Environment* **118**, 339–355. doi:10.1016/j.rse.2011.11.024

Hochstein MP and 5 others (1995) Downwasting of the Tasman Glacier, South Island, New Zealand: changes in the terminus region between 1971 and 1993. *New Zealand journal of geology and geophysics* **38**(1), 1–16.

Howat IM, Joughin I, Fahnestock M, Smith BE and Scambos TA (2008) Synchronous retreat and acceleration of southeast Greenland outlet glaciers 2000–06: ice dynamics and coupling to climate. *Journal of Glaciology* **54**(187), 646–660. doi:10.3189/002214308786570908

Howat IM, Joughin I and Scambos TA (2007) Rapid changes in ice discharge from Greenland outlet glaciers. *Science* **315**(5818), 1559–1561. doi:10.1126/science.1138478

Howat IM, Joughin I, Tulaczyk S and Gogineni S (2005) Rapid retreat and acceleration of Helheim Glacier, east Greenland. *Geophysical Research Letters* **32**(22), 646–660. doi: 10.1029/2005GL024737.

Hugonnet R and 10 others (2021) Accelerated global glacier mass loss in the early twenty-first century. *Nature* **592**(7856), 726–731. doi:10.1038/s41586-021-03436-z

James TD, Murray T, Selmes N, Scharrer K and O'Leary M (2014) Buoyant flexure and basal crevassing in dynamic mass loss at Helheim Glacier. *Nature Geoscience* **7**(8), 593–596. doi:doi.org/10.1038/ngeo2204

Joughin I and 8 others (2008) Ice-front variation and tidewater behavior on Helheim and Kangerdlugssuaq Glaciers, Greenland. *Journal of Geophysical Research: Earth Surface* **113**(F1), F01004. doi: 10.1029/2007JF000837.

Kadota T, Naruse R, Skvarca P and Aniya M (1992) Ice flow and surface lowering of Tyndall Glacier, southern Patagonia. *Bulletin Glacier Research* **10**, 63–68.

Kamb B and 5 others (1994) Mechanical and hydrologic basis for the rapid motion of a large tidewater glacier: 2. interpretation. *Journal of Geophysical Research* **99**(B8), 15231–15244. doi:10.1029/94JB00237

Koppes M and 5 others (2015) Observed latitudinal variations in erosion as a function of glacier dynamics. *Nature* **526**(7571), 100–103. doi:10.1038/nature15385

Laumann T and Wold B (1992) Reactions of a calving glacier to large changes in water level. *Annals of Glaciology* **16**, 158–162. doi:10.3189/1992AoG16-1-158-162

Meier M and 9 others (1994) Mechanical and hydrologic basis for the rapid motion of a large tidewater glacier: 1. Observations. *Journal of Geophysical Research: Solid Earth* **99**(B8), 15219–15229. doi:10.1029/94JB00237

Meier WJ, Grießinger J, Hochreuther P and Braun MH (2018) An updated multi-temporal glacier inventory for the Patagonian Andes with changes between the Little Ice Age and 2016. *Frontiers in Earth Science* **6**(5), 1–21. doi: 10.3389/feart.2018.00062.

Meier MF and Post A (1987) Fast tidewater glaciers. *Journal of Geophysical Research* **92**(B9), 9051. doi:10.1029/JB092iB09p09051

Meier MF, Rasmussen LA and Miller DS (1985) Columbia glacier in 1984: disintegration underway. Technical report, Geological Survey, Tacoma, WA (USA).

Messerli A and Grinsted A (2015) Image georectification and feature tracking toolbox: ImGRAFT. *Geoscientific Instrumentation, Methods and Data Systems* **4**(1), 23–34. doi:10.5194/gi-4-23-2015

Millan R and 10 others (2019) Ice thickness and bed elevation of the Northern and Southern Patagonian Icefields. *Geophysical Research Letters* **46**(12), 6626–6635. doi:10.1029/2019GL082485

Minowa M, Schaefer M, Sugiyama S, Sakakibara D and Skvarca P (2021) Frontal ablation and mass loss of the Patagonian icefields. *Earth and Planetary Science Letters* **561**, 116811. doi:10.1016/j.epsl.2021.116811

Minowa M, Sugiyama S, Sakakibara D and Skvarca P (2017) Seasonal variations in ice-front position controlled by frontal ablation at Glaciar Perito Moreno, the Southern Patagonia Icefield. *Frontiers in Earth Science* **5**(1), 1–15. doi:10.3389/feart.2017.00001

Morlighem M and 5 others (2011) A mass conservation approach for mapping glacier ice thickness. *Geophysical Research Letters* **38**(19), L19503. doi: 10.1029/2011GL048659.

Motyka RJ, Dryer WP, Amundson J, Truffer M and Fahnestock M (2013) Rapid submarine melting driven by subglacial discharge, LeConte Glacier, Alaska. *Geophysical Research Letters* **40**(19), 5153–5158. doi:10.1002/grl.51011

Motyka RJ, Hunter L, Echelmeyer KA and Connor C (2003) Submarine melting at the terminus of a temperate tidewater glacier, LeConte Glacier, Alaska, USA. *Ann. Glaciol.* **36**(1), 57–65. doi:10.3189/172756403781816374

Mouginot J and Rignot E (2015) Ice motion of the Patagonian Icefields of South America: 1984–2014. *Geophysical Research Letters* **42**, 1441–1449. doi:10.1002/2014GL062661

Murray T and 9 others (2015) Dynamics of glacier calving at the ungrounded margin of Helheim Glacier, southeast Greenland. *Journal of Geophysical Research: Earth Surface* **120**(6), 964–982. doi:10.1002/2015JF003531

Muto M and Furuya M (2013) Surface velocities and ice-front positions of eight major glaciers in the Southern Patagonian Ice Field, South America, from 2002 to 2011. *Remote Sensing of Environment* **139**, 50–59. doi: 10.1016/j.res2013.07.034.

Naruse R, Peña H, Aniya M and Inoue J (1987) Flow and surface structure of Tyndall glacier, The Southern Patagonia icefield. *Bulletin Glacier Research* **4**, 133–140.

Naruse R and Skvarca P (2000) Dynamic features of thinning and retreating Glaciar Upsala, a lacustrine calving glacier in southern Patagonia. *Arctic, Antarctic, and Alpine Research* **32**, 485–491. doi:10.2307/1552398

Naruse R, Skvarca P and Takeuchi Y (1997) Thinning and retreat of Glaciar Upsala, and an estimate of annual ablation changes in southern Patagonia. *Annals of Glaciology* **24**, 38–42. doi:10.3189/S0260305500011903

Nick FM, Van der Veen CJ, Vieli A and Benn DI (2010) A physically based calving model applied to marine outlet glaciers and implications for the glacier dynamics. *Journal of Glaciology* **56**(199), 781–794. doi:10.3189/002214310794457344

Nick FM, Vieli A, Howat IM and Joughin I (2009) Large-scale changes in Greenland outlet glacier dynamics triggered at the terminus. *Nature Geoscience* **2**(2), 110–114. doi:10.1038/ngeo394

Nishida K, Satow K, Aniya M, Casassa G and Kadota T (1995) Thickness change and flow of Tyndall Glacier, Patagonia. *Bulletin Glacier Research* **13**, 29–34.

Nuth C and Kääb A (2011) Co-registration and bias corrections of satellite elevation data sets for quantifying glacier thickness change. *Cryospher* **5**(1), 271–290. doi:10.5194/tc-5-271-2011

O'Neel S, Pfeffer WT, Krimmel R and Meier M (2005) Evolving force balance at Columbia Glacier, Alaska, during its rapid retreat. *Journal of Geophysical Research: Earth Surface* **110**(F32250), F32250. doi: 10.1029/2005JF000292.

Parizek BR and 7 others (2019) Ice-cliff failure via retrogressive slumping. *Geology* **47**(5), 449–452. doi:10.1130/G45880.1

Pelto M, Hughes T and Brecher H (1989) Equilibrium state of Jakobshavns Isbræ, West Greenland. *Annals of Glaciology* **12**, 127–131. doi:10.1017/S0260305500007084

Pelto MS and Warren CR (1991) Relationship between tidewater glacier calving velocity and water depth at the calving front. *Annals of Glaciology* **15**, 115–118. doi:10.3189/s0260305500009617

Pfeffer W (2007) A simple mechanism for irreversible tidewater glacier retreat. *Journal of Geophysical Research: Earth Surface* **112**(F3), F03S25. doi: 10.1029/2006JF000590.

Purdie H, Bealing P, Tidey E, Gomez C and Harrison J (2016) Bathymetric evolution of Tasman Glacier terminal lake, New Zealand, as determined by remote surveying techniques. *Global and Planetary Change* **147**, 1–11. doi:10.1016/j.gloplacha.2016.10.010

Raymond C and 5 others (2005) Retreat of Glaciar Tyndall, Patagonia, over the last half-century. *Journal of Glaciology* **51**(173), 239–247.

Rignot E, Forster R and Isacks B (1996) Mapping of glacial motion and surface topography of Hielo Patagónico Norte, Chile, using satellite SAR l-band interferometry data. *Annals of Glaciology* **23**, 209–216. doi:10.3189/S0022143000004147

Rignot E, Rivera A and Casassa G (2003) Contribution of the Patagonia Icefields of South America to sea level rise. *Science* **302**, 434–437, doi:10.1126/science.1087393

Rivera A and Casassa G (2004) Ice elevation, areal, and frontal changes of glaciers from National Park Torres del Paine, Southern Patagonia Icefield. *Arctic, Antarctic, and Alpine Research* **36**(4), 379–389.

Rivera A, Lange H, Aravena JC and Casassa G (1997) The 20th-century advance of glaciar Pio XI, Chilean Patagonia. *Annals of Glaciology* **24**, 66–71. doi:10.3189/S0260305500011952

Rott H, Stuefer M, Siegel A, Skvarca P and Eckstaller A (1998) Mass fluxes and dynamics of Moreno glacier, Southern Patagonia icefield. *Geophysical Research Letters* **25**(9), 1407–1410. doi:10.1029/98GL00833

Sakakibara D (2016) *Ice front variations and velocity changes of calving glaciers in the Southern Patagonia Icefield and northwestern Greenland.* Ph.D. thesis, Hokkaido University.

Sakakibara D and Sugiyama S (2014) Ice-front variations and speed changes of calving glaciers in the Southern Patagonia Icefield from 1984 to 2011. *Journal of Geophysical Research: Earth Surface* **119**(11), 2541–2554. doi:10.1002/2014JF003148

Sakakibara D, Sugiyama S, Sawagaki T, Marinsek S and Skvarca P (2013) Rapid retreat, acceleration and thinning of Glaciar Upsala, Southern Patagonia Icefield, initiated in 2008. *Annals of Glaciology* **54**(63), 131–138. doi:10.3189/2013AoG63A236

Sato Y and 7 others (2022) Land- to lake-terminating transition triggers dynamic thinning of a Bhutanese glacier. *Cryosphere* **16**(6), 2643–2654. doi:10.5194/tc-16-2643-2022

Schaefer M, Casassa G and Loriaux T (2011) Simulating the retreat of the freshwater calving Glacier O'Higgins using a flow line model. In *EGU General Assembly Conference Abstracts*, EGU2011–12379.

Seguinot J (2020) Sentinelflow: automated satellite image workflow for Sentinel-2. doi:10.5281/zenodo.3634077

Shean DE and 6 others2016) An automated, open-source pipeline for mass production of digital elevation models (DEMs) from very-high-resolution commercial stereo satellite imagery. *ISPRS Journal of Photogrammetry and Remote Sensing* **116**, 101–117. doi:10.1016/j.isprsjprs.2016.03.012

Skvarca P, De Angelis H, Naruse R, Warren C and Aniya M (2002) Calving rates in fresh water: new data from southern Patagonia. *Annals of Glaciology* **34**, 379–384. doi:10.3189/172756402781817806

Skvarca P and Naruse R (1997) Dynamic behavior of Glaciar Perito Moreno, southern Patagonia. *Annals of Glaciology* **24**, 268–271. doi:10.3189/S0260305500012283

Skvarca P, Raup B and De Angelis H (2003) Recent behaviour of Glaciar Upsala, a fast-flowing calving glacier in Lago Argentino, southern Patagonia. *Annals of Glaciology* **36**, 184–188.

Skvarca P, Satow K, Naruse R and Leiva JC (1995) Recent thinning, retreat and flow of Upsala Glacier, Patagonia. *Bulletin Glacier Research* **13**, 11–20.

Stearns LA and 6 others (2015) Glaciological and marine geological controls on terminus dynamics of Hubbard Glacier, southeast Alaska. *Journal of Geophysical Research: Earth* **120**(6), 1065–1081. doi:10.1002/2014JF003341

Stearns L and Van der Veen C (2018) Friction at the bed does not control fast glacier flow. *Science* **361**(6399), 273–277.

Sugiyama S and 7 others (2011) Ice speed of a calving glacier modulated by small fluctuations in basal water pressure. *Nature Geoscience* **4**(9), 597–600. doi:10.1038/ngeo1218

Sugiyama S and 7 others (2016) Thermal structure of proglacial lakes in Patagonia. *Journal of Geophysical Research: Earth* **121**(12), 2270–2286. doi:10.1002/2016JF004084

Sugiyama S and 7 others (2021) Subglacial discharge controls seasonal variations in the thermal structure of a glacial lake in Patagonia. *Nature Communications* **12**(1), 1–9. doi:10.1038/s41467-021-26578-0

Sugiyama S, Minowa M and Schaefer M (2019) Underwater ice terrace observed at the front of Glaciar Grey, a freshwater calving glacier in Patagonia. *Geophysical Research Letters* **46**(5), 2602–2609. doi:10.1029/2018GL081441

Trevers M, Payne AJ, Cornford SL and Moon T (2019) Buoyant forces promote tidewater glacier iceberg calving through large basal stress concentrations. *Cryosphere* **13**(7), 1877–1887. doi:10.5194/tc-13-1877-2019

Truffer M and Motyka R (2016) Where glaciers meet water: Subaqueous melt and its relevance to glaciers in various settings. *Reviews of Geophysics* **54**, 220–239. doi:10.1002/2015RG000494

Trüssel BL, Motyka RJ, Truffer M and Larsen CF (2013) Rapid thinning of lake-calving Yakutat Glacier and the collapse of the Yakutat Icefield, southeast Alaska, USA. *Journal of Glaciology* **59**(213), 149–161. doi:10.3189/2013J0G12J081

Tsutaki S, Sugiyama S, Nishimura D and Funk M (2013) Acceleration and flotation of a glacier terminus during formation of a proglacial lake in Rhonegletscher, Switzerland. *Journal of Glaciology* **59**(215), 559–570. doi:10.3189/2013JoG12J107

Ultee L, Felikson D, Minchew B, Stearns LA and Riel B (2022) Helheim Glacier ice velocity variability responds to runoff and terminus position change at different timescales. *Nature Communications* **13**(1), 1–21. doi:10.1038/s41467-022-33292-y

van der Veen C (1998) Fracture mechanics approach to penetration of bottom crevasses on glaciers. *Cold Regions Science and Technology* **27**(3), 213–223. doi:10.1016/S0165-232X(98)00006-8

van der Veen C (2002) Calving glaciers. *Progress in Physical Geography* **26**(1), 96–122. doi:10.1191/0309133302pp327ra

van Dongen EC and 10 others (2021) Thinning leads to calving-style changes at Bowdoin Glacier, Greenland. *Cryosphere* **15**(2), 485–500. doi:10.5194/tc-15-485-2021

Walter F and 5 others (2010) Iceberg calving during transition from grounded to floating ice: Columbia Glacier, Alaska. *Geophysical Research Letters* **37**(15), L15501. doi: 10.1029/2010GL043201.

Walter A, Lüthi MP and Vieli A (2020) Calving event size measurements and statistics of Eqip Sermia, Greenland, from terrestrial radar interferometry. *Cryosphere* **14**(3), 1051–1066. doi:10.5194/tc-14-1051-2020

Warren CR and 5 others (1995a) Characteristics of tide-water calving at Glaciar San Rafael, Chile. *Journal of Glaciology* **41**(138), 273–289. doi:10.3189/S0022143000016178

Warren C and Aniya M (1999) The calving glaciers of southern South America. *Global and Planetary Change* **22**(1–4), 59–77. doi:10.1016/S0921-8181(99)00026-0

Warren C, Benn D, Winchester V and Harrison S (2001) Buoyancy-driven lacustrine calving, Glaciar Nef, Chilean Patagonia. *Journal of Glaciology* **47**(156), 135–146. doi:10.3189/172756501781832403

Warren CR, Greene DR and Glasser NF (1995b) Glaciar Upsala, Patagonia: rapid calving retreat in fresh water. *Journal of Glaciology* **21**, 311–316. doi:10.3189/S0260305500015998

Warren CR and Kirkbride MP (2003) Calving speed and climatic sensitivity of New Zealand lake-calving glaciers. *Journal of Glaciology* **36**, 173–178. doi:10.3189/172756403781816446

Watson D (1999) The natural neighbor series manuals and source codes. *Computers & Geosciences* **25**(4), 463–466. doi:10.1016/S0098-3004(98)00150-2

Weertman J (1974) Stability of the junction of an ice sheet and an ice shelf. *Journal of Glaciology* **13**(67), 3–11. doi:10.3189/S0022143000023327

Zamora R and 8 others (2009) Airborne radar sounder for temperate ice: initial results from Patagonia. *Journal of Glaciology* **55**(191), 507–512. doi:10.3189/002214309788816641
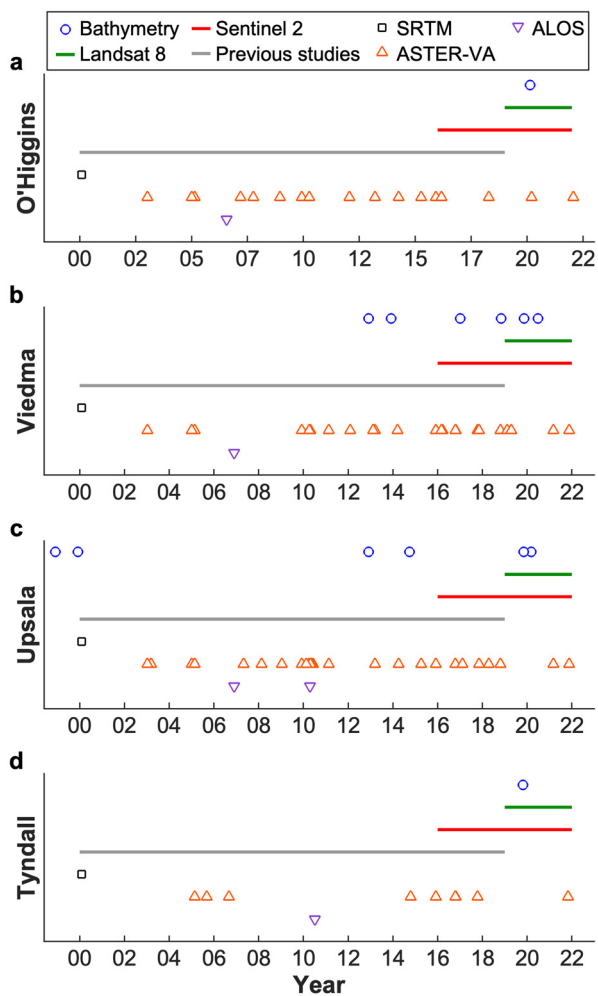
Appendix

Figure 12. An overview of the available dataset for (a) O'Higgins, (b) Viedma, (c) Upsala and (d) Tyndall glaciers. The timing of the bathymetry survey is indicated by the blue circle. The horizontal green and red bars indicate the available period of optical Sentinel 2 and Landsat 8 images used for analysing the ice-front position and surface ice speed in this study. We combined data analysed by using Landsat 5, 7 and 8 images in previous studies (Sakakibara and Sugiyama, 2014; Minowa and others, 2021) as indicated by a grey horizontal bar. Black squares, orange triangles and purple triangles indicate available DEMs obtained by SRTM mission, ASTER satellite and ALOS satellite, respectively.
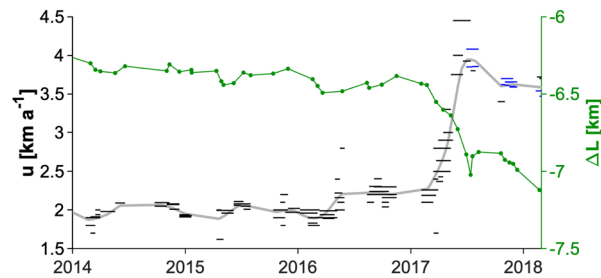

Figure 13. Surface ice speed and ice front position observed at Glaciar O'Higgins between 2014 and 2018. Grey line indicates smoothed surface ice speed using a Gaussian smoothing routine with a time window of 90 days.
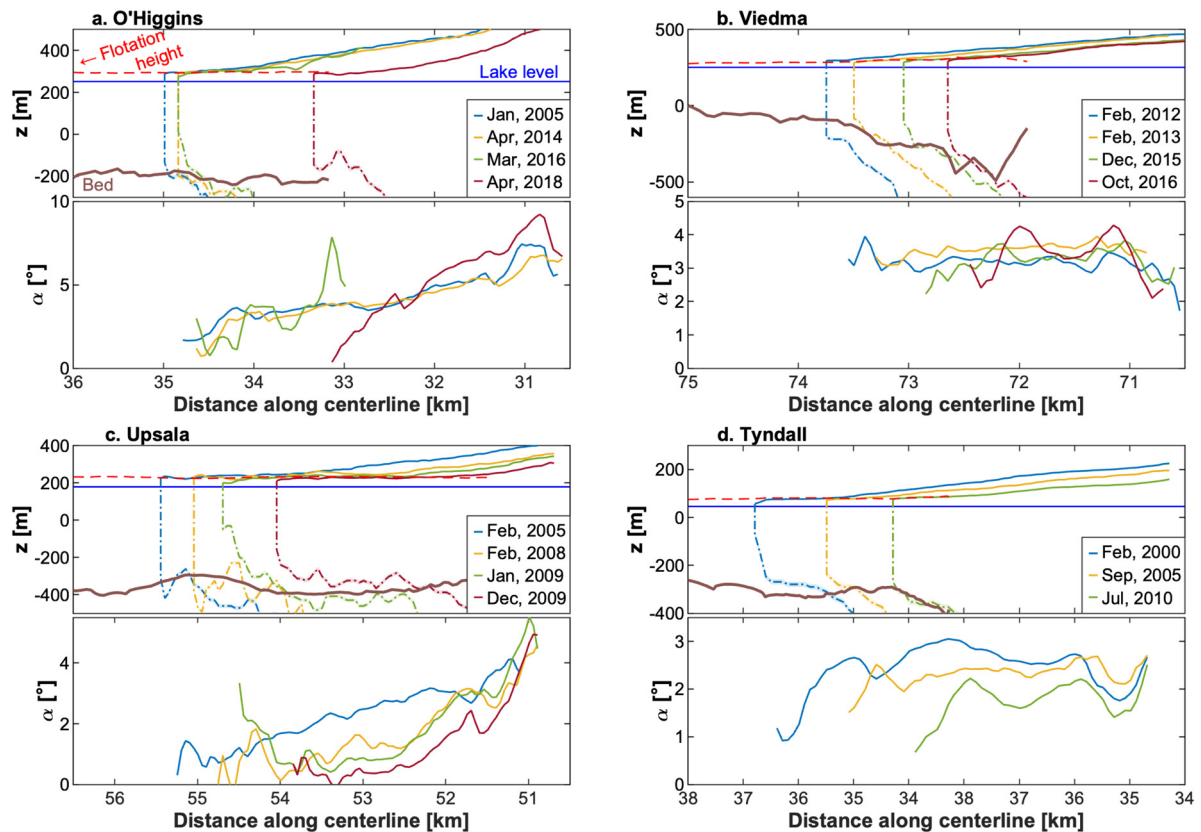
Figure 14. Longitudinal profiles of the ice surface elevations and slopes along the centreline at every 50 m in the horizontal interval for (a) Glaciar O'Higgins, (b) Glaciar Viedma, (c) Glaciar Upsala and (d) Glaciar Tyndall. The colour of the lines indicates the date. Red, blue and brown lines represent the flotation height, lake level and bed elevation, respectively. The dot-dashed line is the glacier base assuming hydrostatic equilibrium. The surface slope was calculated after applying the moving average on the surface elevation with a span of 2 km.
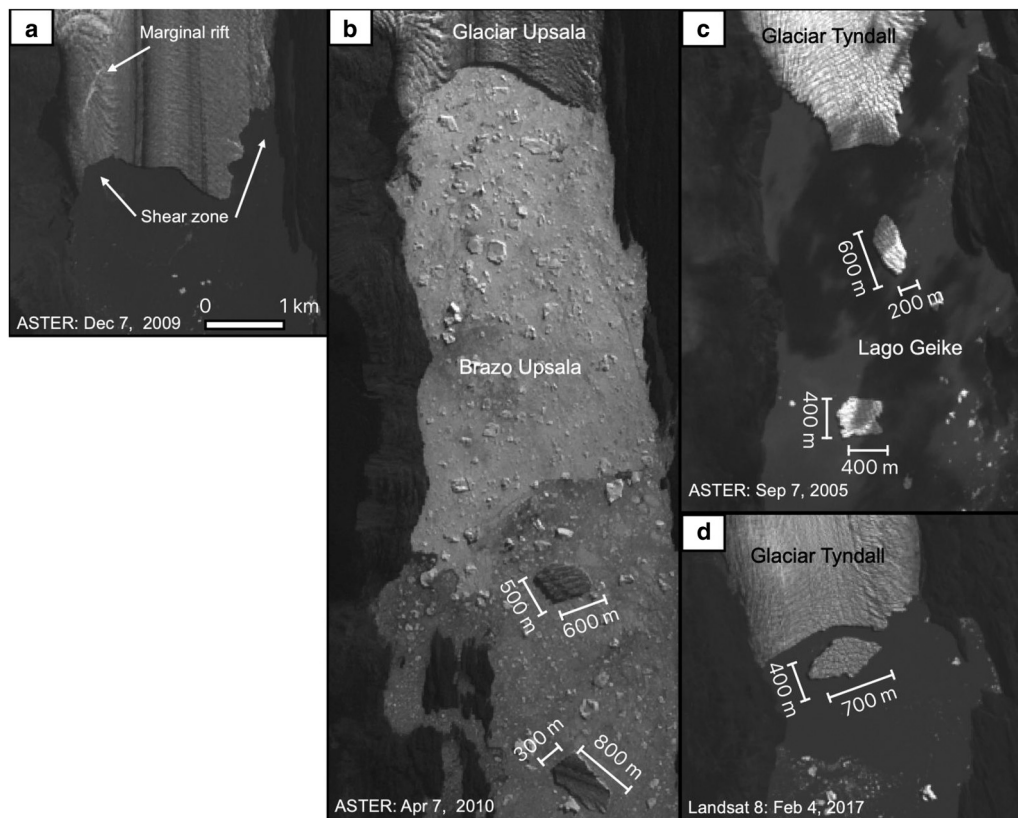

Figure 15. Tabular icebergs observed at (a) and (b) Glaciar Upsala, and (c) and (d) at Glaciar Tyndall. Note that the scale of the satellite images is different depending on the glacier.